Construction and Building Materials 440 (2024) 137396

Contents lists available at ScienceDirect

Construction and Building Materials

journal homepage: www.elsevier.com/locate/conbuildmat

A multi-performance comparison between lime, cementitious and alkali-activated TRM systems: Mechanical, environmental and energy perspectives

Jacopo Donnini [a,*], Alessandra Mobili [a], Gianluca Maracchini [b], Gianluca Chiappini [c], Francesca Tittarelli [a], Valeria Corinaldesi [a]

[a] Department of Science and Engineering of Matter, Environment and Urban Planning, Università Politecnica delle Marche, Via Brecce Bianche 12, Ancona 60131, Italy
[b] Department of Civil, Environmental and Mechanical Engineering, Università di Trento, Via Mesiano 77, Trento 38123, Italy
[c] Faculty of Engineering, Università E-Campus, Italy

ARTICLE INFO

Keywords:
Textile reinforced mortar
FRCM
Geopolymer
Alkali-activated materials
Glass fibers
Basalt fibers
LCA
Energy
CO2 emission

ABSTRACT

The combined need to propose new solutions for the structural reinforcement of existing buildings and for the reduction of CO_2 emissions is leading to the development of more sustainable composite materials, such as those based on alkali-activated mortars (AAM). In this study, different formulations of AAM, based on metakaolin or fly ash, have been evaluated as possible matrices for Textile Reinforced Mortar (TRM) systems. Two different bidirectional textiles, made of AR glass or basalt fibers, were used as internal reinforcement. The physical-mechanical properties of TRM systems based on AAM were evaluated and compared with those of commercial systems with cementitious or lime-based matrices. Direct tensile tests on TRM coupons and shear bond tests on clay brick substrates were carried out. Then, their energy and environmental-related performance have been compared. Results showed that alkali-activated matrices can be very promising and eco-friendly alternative solutions to traditional mortars in TRM systems.

1. Introduction

In recent years Textile Reinforced Mortar (TRM), also called Fabric Reinforced Cementitious Matrix (FRCM), has emerged as a promising alternative to conventional reinforcement systems, such as steel bars, welded wire mesh, and Fiber Reinforced Polymers (FRP). TRM consists of a grid made of continuous fibers (usually glass, basalt, or carbon fibers) embedded in a cement- or lime-based mortar matrix. It is widely used to repair and strengthen existing structures, both masonry and reinforced concrete, and it is particularly suited for seismic retrofitting, as it can enhance the ductility and energy dissipation capacity of reinforced elements [1–4]. This innovative technology is gaining popularity among engineers and contractors due to its many advantages, such as easy handling, low weight, fast installation, applicability on wet surfaces, high tensile strength, corrosion resistance, and low cost.

Commercially available TRM systems are usually made up of natural hydraulic lime, Ordinary Portland Cement (OPC), or a combination thereof. The inorganic matrix plays a fundamental role since it is responsible for the transfer of stresses between the reinforced element (usually masonry or concrete) and the reinforcing textile of the system [5–7]. For this reason, the physical-mechanical compatibility between mortar and support is essential to ensure the effectiveness of the reinforcing system. There are several inorganic matrices available on the market, but usually they are divided into two categories, depending on whether the reinforcement is to be applied to masonry or concrete structures. Mortars for masonry strengthening are usually of class R1 or R2 (with $R_c \geq 10$ MPa and $R_c \geq 15$ MPa, respectively), while those for reinforced concrete are R3 or R4 (with $R_c \geq 25$ MPa and $R_c \geq 45$ MPa, respectively), according to UNI EN 1504–3:2006. Commonly, lime-based mortars are preferred for rehabilitation of historical buildings, being more compatible with the masonry substrate. Conversely, cementitious matrixes are more suitable for concrete substrates.

Recently, interest has turned toward the development of alternative inorganic matrices for TRM systems, such as alkali-activated mortars (AAMs). AAMs have been gaining increasing attention as a potential alternative to conventional cementitious mortars due to their lower carbon footprint [8–10]. The saving of CO_2 emitted by using alkali-activated binders, compared to OPC, is estimated between 30 %

* Corresponding author.
E-mail address: jacopo.donnini@staff.univpm.it (J. Donnini).

https://doi.org/10.1016/j.conbuildmat.2024.137396
Received 29 February 2024; Received in revised form 25 June 2024; Accepted 7 July 2024
Available online 13 July 2024

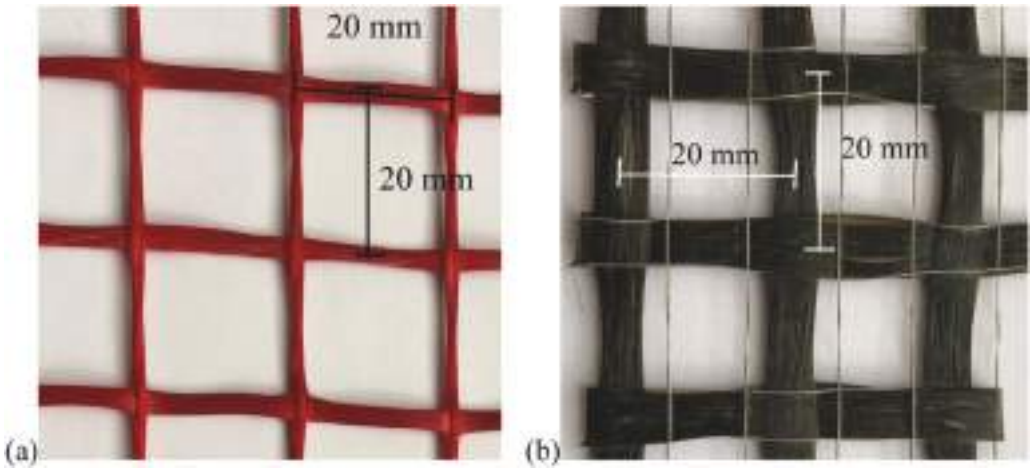

Fig. 1. (a) Glass and (b) basalt textiles employed as TRM reinforcement.

and 80 %, depending on the type of precursor and activator used and on the LCA methodology adopted [11,12]. One of the key factors influencing the properties of AAMs is the type and concentration of the activator used. Common activators include sodium hydroxide, potassium hydroxide, and sodium silicate [13,14]. The type and concentration of the activator can be tailored to achieve specific physical and mechanical properties, such as workability, setting time, strength and durability, making AAMs highly customizable.

Further advantages in the use of AAMs are related to their high mechanical strength (similar or superior to conventional mortars), good adhesion to concrete substrates [15], better resistance to high temperatures [9] and improved durability under a variety of environmental conditions [16–18]. Moreover, the low modulus of elasticity of some AAMs makes them very interesting for applications on masonry structures. Considering AAMs for TRM applications, sometimes called Textile Reinforced Alkali-Activated Mortars (TRAAMs) [19], recent studies showed the feasibility of using different matrices. However, the literature on this topic is still very limited and mainly focused on concrete strengthening, while studies regarding the application on masonry elements are still lacking.

Carabba et al. [20] investigated the use of coal fly ash geopolymer mortars coupled with high-strength galvanized steel fibers. Experimental results showed a good compatibility between the geopolymer mortar and the concrete substrate. Moreover, the interfacial bond between matrix and fiber increases as the concentration of the NaOH activating solution decreases, thus the compressive strength of the mortar decreases. The possibility of using textile-reinforced geopolymer mortar (TRGM) to strengthen concrete beams was investigated by Zhang et al. [21]. TRGMs showed to be very promising, by enhancing the shear capacity of concrete beams by 47 % and 106 % when using one or two layers of TRGM, respectively, while the effective strain of the textile was comparable to or even higher than the corresponding strain developed with conventional mortars. John et al. [22] experimentally investigated the tensile and shear bond properties on concrete substrates of TRM systems made with a fly ash-slag-based geopolymer mortar reinforced with PVA fibers. All specimens failed by matrix cracking followed by textile rupture in tensile tests, while shear bond tests indicated a good bond between textile and concrete substrate. The mechanical behavior of TRM systems based on fly ash, metakaolin and ladle furnace slag was investigated by Arce et al. [19] through tensile and shear bond tests on concrete substrates. TRM based on high calcium fly ash showed a poor bond with concrete substrate while TRM based on metakaolin showed better performances both in terms of tensile strength and bond capacity. Cholostiakow et al. [23] compared the behavior of metakaolin geopolymer and cement-based mortars to strengthen masonry wallets with basalt and glass textiles. Geopolymer-based systems proved to be suitable for retrofitting applications, showing mechanical performances comparable to or better than cementitious mortars. Candamano et al. [24] activated fly ash, slag and biomass ash to produce a geopolymer mortar coupled to basalt fibers to strengthen masonry prisms. Results were encouraging although a better dimensional stability of the matrix would have been desirable. Tamburini et al. [25] studied the use of a metakaolin/slag geopolymer mortar to bond different reinforcing fiber nets and fabrics to soft mud and strong extruded clay bricks. They found out that all the fiber reinforcements (basalt, glass, carbon, and steel) had excellent adhesion to soft mud clay bricks since the failure obtained by pull-off tests occurred within the substrate. Moreover, results on composites applied to strong extruded clay bricks showed adhesive strength comparable to that of the unreinforced system, except for the one manufactured with glass fibers where the lower strength was related to the closer spacing of the fibers bundles. Mobili et al. investigated the bond behavior of fly ash [26] and metakaolin [27] geopolymer mortars compared to cementitious mortars with the same mechanical strength class on red clay bricks. They found out that the higher the strength class the higher the adhesive strength to the substrate.

In this study, the possibility of using different AAMs, based on fly ash (FA) or metakaolin (MK), coupled with glass or basalt textiles for TRM applications, has been preliminary evaluated. The initial objective was to develop AAMs with physical-mechanical properties comparable to those of lime (R1 class) and cement-based (R3 class) commercially available mortars for TRM systems. Then, once the composition of the matrices was defined, mechanical characterization tests on TRAAM coupons were carried out and results were compared with those of TRM realized by using commercial mortars. The performances of the newly developed TRAAM were also evaluated through single-shear bond tests on red clay brick substrates. Lastly, a comparison in terms of the Embodied Energy (EE) and Global Warming Potential (GWP) between the different TRM systems has also been carried out in relation to the obtained mechanical performance to provide a multi-performance perspective. The advantages and possible drawbacks of using different matrices have been finally highlighted and discussed.

2. Materials

2.1. Reinforcement textiles

Two different commercially available bidirectional textiles have been investigated as TRM reinforcement (Fig. 1). The first one is made of Alkali-Resistant (AR) glass fibers, pre-impregnated with SBS (styrene-butadiene-styrene), with net weight of 240 g/m^2 and total weight of 320 g/m^2. The second textile is made of basalt fibers, pre-impregnated with a polyester-based coating, with net weight of 365 g/m^2 and total

Table 1
Properties of the reinforcement textiles (from manufacturer).

Reinforcement textile	Net weight (g/m^2)	Total weight (g/m^2)	Cross sectional area of single yarn, A_y (mm^2)	Yarn tensile strength (MPa)	Yarn modulus of elasticity (GPa)
Glass	240	320	0.998	1118	66
Basalt	365	420	1.33	1402	72

weight of 420 g/m^2. The main properties of the textiles are reported in Table 1.

2.2. Geopolymer mortars

Geopolymer mortars were manufactured with two different aluminosilicate precursors, namely fly ash (FA) and metakaolin (MK). The former was a class F fly ash provided by the Italian company General Admixture S.p.A., the latter was commercially available as Metastar® 501 and supplied by Imerys Minerals Ltd. FA had a specific surface area (SSA) of 5000 cm^2/g and mean particle size of 20 μm, whereas MK had a SSA of 140000 cm^2/g and mean particle size of 3 μm. In order to increase the available aluminum for geopolymerization, a low amount of calcium aluminate cement (CAC) produced by Kerneos Inc. was added to mortars manufactured with FA. CAC had a SSA comprised between 2850 and 3450 cm^2/g and mean particle size around 10 and 20 μm. To activate mortars, a blend of sodium silicate (SS), KOH and water was used. SS had a SiO_2/Na_2O molar ratio of 2.1 and was produced by Ingessil S.r.l., whereas the hydroxide was a 50 wt% solution of KOH in water. The activating solution was prepared 24 h before the test to allow it to cool to room temperature and permit a good polymerization process. A calcareous sand with maximum diameter of 3 mm and water absorption of 3.4 % by mass provided by Esincalce S.r.l. was used as aggregate.

Two mortars were prepared with FA and CAC, while two other mortars were prepared with MK according to the mix proportions reported in Table 2.

2.3. Commercial mortars

Two different commercial mortars for TRM applications have been considered in this study. The first one is a lime-based mortar (strength class R1, according to the UNI EN1504–3:2006 standard), specifically designed for strengthening interventions on masonry walls. It is based on pure natural lime NHL 3.5, a mineral binder, and a mix of siliceous and limestone sand with a maximum diameter equal to 1.4 mm. The second one is a cement-based mortar (strength class R4 according to the above-mentioned standard) with a maximum diameter of the aggregates equal to 0.5 mm.

3. Methods

3.1. Physical-mechanical characterization of mortars

After mixing, the consistence of fresh mortars was assessed by means of the flow table test and expressed in terms of mean diameter after jolting the table for 15 times, according to UNI EN 1015–3:2019. Mortar prisms with dimensions of 40x40x160 mm^3 were then cast, cured at laboratory conditions (20 ± 2 °C, RH = 65 ± 5 %) for 28 days and tested according to UNI EN 1015–11:2019. The dynamic modulus of elasticity was measured through an ultrasonic digital indicator tester (PUNDIT) with a resolution of 0.1 μs, according to UNI EN 12504–4:2021.

3.2. Tensile tests on TRM coupons

A total of 48 TRM coupons (380x60x10 mm^3) have been

Table 2
Mix proportions of alkali-activated mortars (g/L).

Mixture	Sand	Mixing water	FA	CAC	MKK	Activators			w/b
						SS	KOH	Water	
FAK_1	1409	-	480	42	-	157	62	94	0.34
FAK_2	1390	8	474	41		175	175	-	0.28
MKK_1	1090	44	-	-	404	242	65	178	0.71
MKK_2	1098	51	-	-	407	244	122	122	0.64

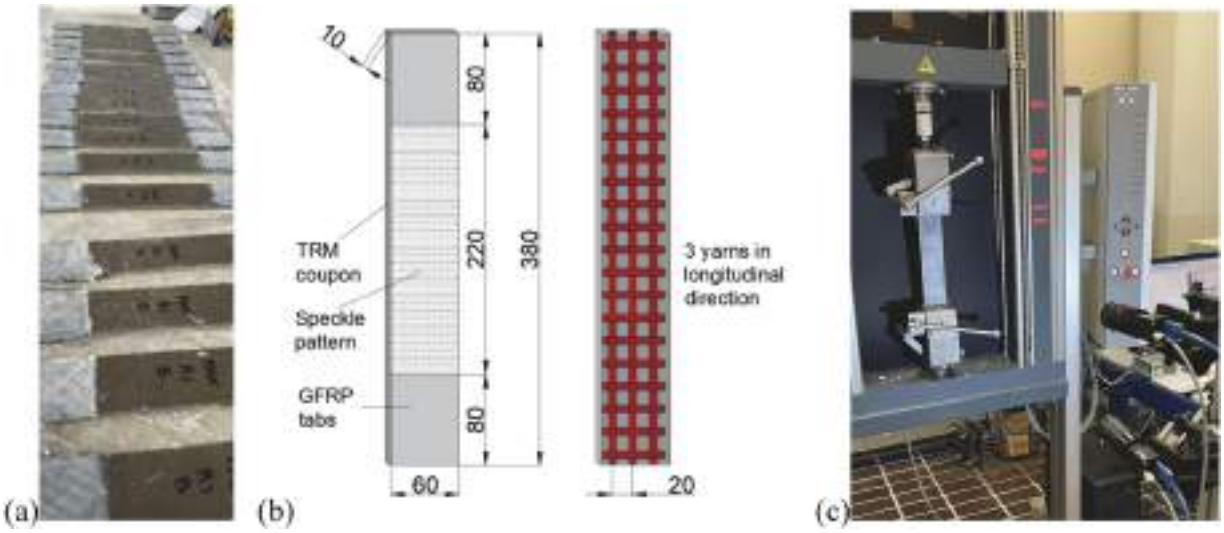

Fig. 2. Direct tensile test: (a) preparation of TRM coupons, (b) coupon's dimensions and (c) test setup with DIC acquisition system.

Table 3
Stereo-DIC settings for tensile tests.

CMOS cameras	FLIR Blackfly S BFS-U3-88S6M-C
Lens	Fujinon CF50ZA-1S
Image resolution	2160×4096 pixels, 8 bit
Field of view	142×270 mm
Pixel to mm conversion	1 pixel = 0.066 mm
Stereo-angle	14°
Stand-off distance	950 mm
Patterning technique	Matt white spray paint base coat with black speckles
DIC technique	Stereo correlation
DIC software	3D-DIC software developed with matlab
Image filtering Gaussian	Gaussian, 5×5 pixel kernel
Subset size	32×32
Matching criterion	Zero-normalized sum of square differences (ZNSSD)
Interpolant	Bi-cubic spline
Stereo transformation	Affine
Strain computation	Gradient

manufactured by combining the six different mortars with a layer of bidirectional glass (G) or basalt (B) textile. Four specimens for each combination of mortar and textile have been manufactured and tested. The textile comprises 3 yarns in the longitudinal direction, and it is embedded within the mortar with total thickness of 10 mm. Coupons were cured for 28 days at laboratory conditions (20 ± 2 °C; 65 ± 5 % R. H.) before testing. GFRP tabs (80×60 mm) were epoxy bonded at the ends of each coupon to improve grip, prevent slipping from the testing machine and to avoid localized failure at the gripping areas.

Tensile tests were conducted using a Zwick/Roell Z050 machine under displacements control, with a crosshead speed of 0.5 mm/min; the testing machine was equipped with a 50 kN load cell. Stereo- DIC (Digital Image Correlation) was used to measure axial strain and to monitor the formation of cracks during the test. Stereo-DIC was employed to avoid the errors arising from out-of-plane motion, a common issue in 2D-DIC measurement systems as identified by Sutton et al. [28]. The images were captured using two digital cameras (FLIR Blackfly S BFS-U3–88S6M-C model) equipped with lenses with a focal length of 50 mm and synchronized with the force measured by the load cell. The cameras were placed with an angle of 14°, and a led lamp to ensure a proper illumination was used. The setup was optimized following the guidelines of the International Digital Image Correlation Society [29] to minimize experimental uncertainties, as investigated by Badaloni et al. [30]. The specimens geometry and the complete experimental setup are shown in Fig. 2 while the stereo-DIC settings are summarized in Table 3.

A high-contrast random speckle pattern was created on the specimen's surface by applying a thin layer of random black spray paint on a white background. The images were post-processed by an in-house developed DIC Software with Matlab®: description of the algorithm used herein for the correlation can be found in [31] and applications example in [32–36]. The correlation method adopted is based on global DIC, the image of the undeformed sample is divided in a number of subimages (or subsets, size 32×32 pixel) each one containing a portion of speckles; as specimen deforms, the speckle patterns deform as well.

The displacements of all grid nodes were obtained by finding a mapping that best correlates the shape of the deformed subsets with the undeformed ones, while considering the epipolar constraint between the two cameras [36]. The zero-normalized sum of square difference

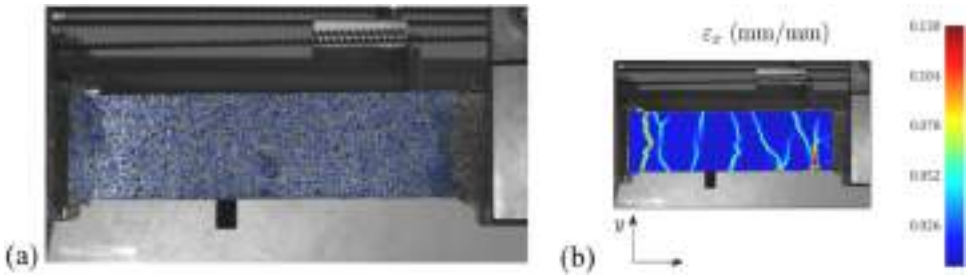

Fig. 3. Post-processing of the images: (a) subsets grid in stereo-DIC; (b) example of a longitudinal strain e_x map where the crack pattern on the surface of the specimen is visible.

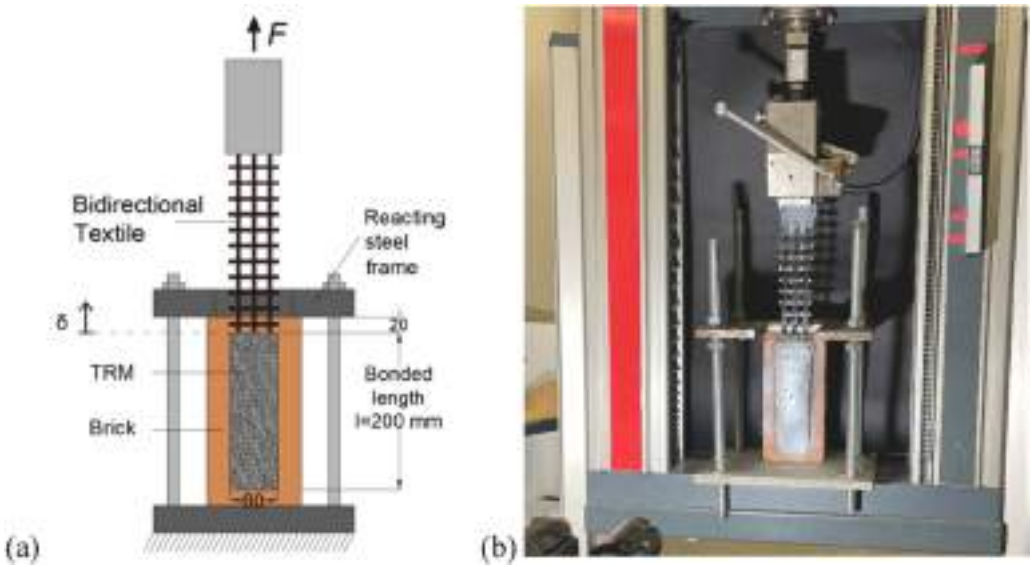

Fig. 4. Single shear bond test: (a) specimen' dimensions and (b) test setup.

(ZNSSD) criterion was adopted to avoid the effects of lighting offset and inhomogeneity. After determining the node displacements, the deformations (Hencky strain ε_x, ε_y, and ε_{xy}) are computed using the Cauchy-Green theory, considering large displacements and large deformations theory. Fig. 3a shows an image of the specimen with a grid of measurement points. In Fig. 3b, the contour map of the axial strain distribution is superimposed on the acquired picture, revealing the visible cracks that have formed on the surface of the specimen.

The average of the axial strain, measured across the entire surface, was employed to derive stress-strain curves that depict the tensile behavior of the TRM coupons.

3.3. Single shear bond tests

A total of 18 shear bond tests have been carried out, in order to investigate the bond capacity of the six different matrices to clay brick substrates. The dimensions of specimens and the test setup are shown in Fig. 4. The TRM strip had a width of 60 mm, comprising three basalt yarns in the longitudinal direction, and a bonded length of 200 mm. The strip was spaced from the top edge of the brick by 20 mm to avoid stress concentration. Bricks were saturated (immersion in water for 24 hours) before applying the TRM strip. GFRP tabs with dimensions of 60×100 mm^2 were then epoxy bonded to the end of the basalt textile to improve the grip during the test and to redistribute stresses between the yarns. Specimens were cured for 28 days at laboratory conditions (20 ± 2 °C; 65 ± 5 % R.H.) before testing.

Shear bond tests were carried out with a universal testing machine Zwick Z050 with maximum capacity of 50 kN. The clay brick was restrained by a steel frame anchored to the testing machine. Tests were conducted under displacement control at 0.5 mm/min. DIC was used to monitor the deformations of the inorganic matrix, as well as the formation of cracks. Instead, for measuring the relative displacement of the fabric with respect to the clay brick (δ), an optical grid method was used [36–38]. This procedure is based on the use of some markers placed on the yarns of the fabric and on the steel frame. After calibrating the cameras, stereoscopic algorithms are employed to compute the 3D coordinates of the grid points in a global reference system. These coordinates are then used to calculate, through the difference, the relative displacement of the fabric with respect to the clay brick (referred to the arrow in Fig. 4).

3.4. Energy and environmental performance

In this study, a comparison in terms of the Embodied Energy (EE) and Global Warming Potential (GWP) between the different TRM systems has been carried out. The focus is on the impacts and energy consumption related to the material production excluding the impacts from transportation since they vary and depend on other influencing factors such as distance, type of engine, and raw materials location [39]. To this aim, the energy and CO_2 emission data for each TRM component are gathered from different sources such as the relevant Environmental Product Declarations (EPDs), scientific databases, and literature.

In particular, the embodied energy and CO_2 emissions related to the two commercial mortars (LIME and CEM) and the glass and basalt fiber meshes (G-textile and B-textile, respectively) have been derived from related EPDs and relevant literature. For the geopolymer mortars, instead, the data are derived from the literature and databases [40], as reported in the following subsections. It should be noted that the impact of water is considered negligible [41,42].

3.4.1. Embodied energy of TRM constituents

To compute the overall energy needed to produce the investigated geopolymer mixes, the embodied energy of primary or supplementary materials, aggregates, and the activating solution should be evaluated.

Concerning waste materials, their production requires relatively low energy compared to other components. In previous studies, it was assumed that the energy needed for supplementary cementitious materials (SCMs) production was zero when calculating the total energy for one cubic meter of concrete [43,44]. However, energy is expended during the collection, milling, and grinding processes to achieve a specific size distribution. Therefore, an energy value should be considered for a more accurate comparison and estimation. In [45,46], the energy required to produce one metric ton of FA is estimated at 0.033 GJ/t. Similarly, for virgin SCMs like MKK, the energy requirement is higher, with a typical value of 2.5 GJ/t as reported in [47].

Aggregates, both fine and coarse, represent a large volume component in AAM, affecting stiffness (modulus of elasticity) and, therefore, the dimensional stability (creep and shrinkage) [48]. Some previous studies excluded energy associated with aggregates in their calculations, considering that the compared mixes (OPCC and AAM) contained similar aggregate volumes in their mixtures [43,49]. However, due to differences in the base materials considered in this study, the impact of aggregates has also been considered. In particular, the energy consumption related to the production of one ton of fine aggregates is estimated as 0.083 GJ/t, according to [50].

Finally, activating solutions are the primary contributors to energy consumption [43,51]. In particular, the energy needed to produce sodium silicate (SS, 48 % solid) is approximately 5.371 GJ/t [52]. In our case, a scaled value of 4.9 GJ/t is considered for the SS 44 % solid. Similarly, for KOH, a value of 15.70 GJ/t is assumed, derived from the ecoinvent v.3 database and scaled to take into account the actual solid percentage. In Table 4 and Fig. 5, a summary of the energy required for constituent materials, used to estimate the energy of the resulting mixtures, is reported.

Table 4
Required energy and CO_2 emissions of TRM constituent materials. SS and KOH solutions are referred to a 44 and 50 % content, respectively.

Material	EE [GJ/t]	Ref.	GWP [kgCO_2eq/kg]	Ref.
LIME (pre-mixed)	2	EPD	0.19	EPD
CEM (pre-mixed)	3.54	EPD	0.34	EPD
G-Textile	95.34	EPD	4.5	EPD
B-Textile	47	[57], EPD	2.25	[57], EPD
FA	0.033	[45,46]	0.004	[46,47,50,53]
CAC	6.83	EPD	0.962	EPD
MKK	2.5	[47]	0.33	[46,47,50,53]
SS	4.9	[52]	0.33	[51]
KOH	15.70	ecoinvent	0.90	ecoinvent
Sand	0.083	[50]	0.012	[50]

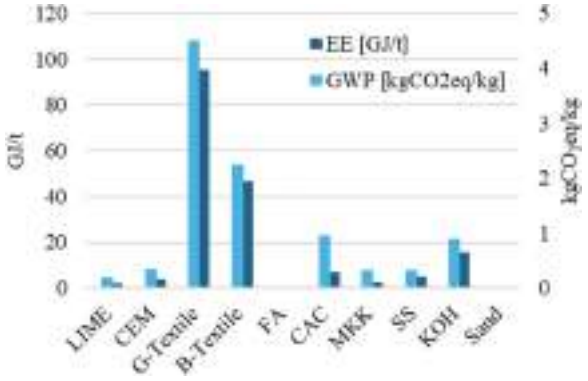

Fig. 5. Required energy and GHG emissions of TRM constituent materials.

Table 5
Mechanical and physical properties of matrices.

Mortar	Days of curing	Compressive strength $\sigma_{c,m}$ (MPa)	Flexural strength $\sigma_{f,m}$ (MPa)	Modulus of elasticity E_m (GPa)	Unit weight (g/cm^3)	Flow value (mm)
FAK_1	7	21.8	6.8	-	-	155
	28	27.4	8.6	24.6	2.27	
FAK_2	7	15.1	5.9	-	-	135
	28	20.2	6.1	23.4	2.34	
MKK_1	7	8.8	1.7	-	-	165
	28	8.8	1.7	8.3	1.93	
MKK_2	7	21.4	3.5	-	-	140
	28	22.7	3.9	10.7	2.04	
LIME	7	5.4	2.1	-	-	120
	28	9.5	3.6	10.1	1.71	
CEM	7	34.2	5.9	-	-	130
	28	43.8	6.9	24.1	2.13	

3.4.2. Embodied CO_2 emissions of TRM constituents

Due to the energy-intensive processes involved in producing materials, such as the use of diesel, electricity, liquid petroleum gas, explosives, and coal, significant CO_2 emissions are released into the atmosphere. Generally, OPC results in higher emissions compared to FA and MKK. Aggregates have relatively low energy requirements during production, resulting in relatively low CO_2 emissions. The CO_2 emissions for FA and MKK are approximately 0.004 and 0.33 kgCO_2e/kg, respectively [46,47,50,53]. Concerning sand, in [41] the authors reported a value of 0.012 kgCO_2e/kg.

Activating solutions, like SS, require substantial energy for their production, leading to significant emissions. SS generates emissions ranging from 0.30 to 0.42 kgCO_2e/kg [52,54]. In [51], the authors reported a value of 1.514 kgCO_2e/kg for sodium silicate, which includes emissions associated with transportation (0.292 kgCO_2e/kg). However, since this study does not consider transportation effects, we excluded the emissions related to transportation, resulting in a net value of 1.222 kgCO_2e/kg. It is worth noting that the authors considered the total emissions of sodium silicates, which is misleading, as sodium silicates typically consist of a solid content between 37 % and 44 % [55,56]. Recently, in [41] the authors reported a lower value equal to 0.74 kgCO_2e/kg, which reflects the most recent data based on European manufacturers. Accordingly, in this study, considering a SS 44 % solid, a scaled value of 0.33 kgCO_2e/kg is assumed. Similarly, a value of 0.9 kgCO_2e/kg is assumed for KOH, derived from the ecoinvent v.3 database and adequately scaled to reflect the solid percentage. Table 4 and Fig. 5 summarize the CO_2 emission for constituent materials in AAC and OPCC, used to estimate the total emission of the resulting mortars.

4. Experimental results and discussion

4.1. Physical-mechanical properties of mortars

Mechanical properties of mortars used as matrices for TRM systems may vary depending on the element to be strengthened, usually between 10 and 20 MPa in compression for masonry structures and >30 MPa for concrete structures. However, some studies showed that even matrices with lower mechanical strengths (thermal insulating mortars), reinforced with glass or basalt textiles, can be effective to strengthen masonry structures [58,59]. The properties of TRM matrices in the fresh state are also of fundamental importance to allow an easy application of the mortar on vertical and overhead surfaces (floors or beams) and to guarantee a correct stress transfer between the substrate and the reinforcing textile. The flow value (evaluated according to UNI EN 1015–3:2007 and UNI EN 1015–6:2007) of commercial mortars for TRM applications is usually between 120 and 150 mm. In this study we tried to develop geopolymer mortars with flowability properties similar to those of commercial mortars. However, the intrinsic nature of geopolymers and the lack of effective additives for this kind of matrices make it more difficult to optimize the rheology while maintaining adequate mechanical properties. Flow values reported in Table 5 showed that geopolymer mortars had higher flowability compared to lime and cement-based mortars. In particular, FAK_2, MKK_2, LIME and CEM had a flowability between 120 and 140 mm (rigid consistency), while FAK_1 and MKK_1, produced with a higher w/b ratio, therefore, a higher water content, provided a plastic consistency.

Results of compressive and bending tests on mortar matrices are reported in Table 5 and Fig. 6. CEM mortars showed the highest compressive strength at 28 days, equal to 43.8 MPa, while FAK_1 had the highest flexural strength, equal to 8.6 MPa. Both FAK mortars have a modulus of elasticity similar to that of CEM. MKK_1 had compressive strength and modulus of elasticity comparable to that of LIME matrices, but a lower flexural strength. MKK_2 had flexural strength at 28 days and modulus of elasticity comparable to LIME matrices, but a higher compressive strength. Due to the intrinsic properties of the materials it is very challenging to design matrices with perfectly comparable physical-mechanical properties. However, for the purposes of this research, and with regards to characterization tests on TRM systems, it seems

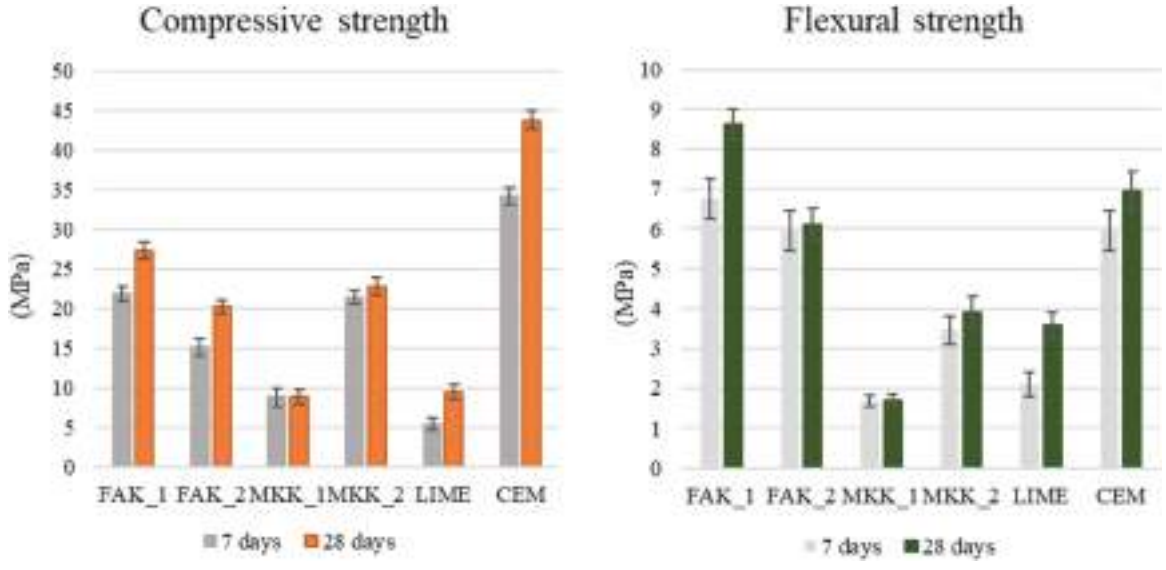

Fig. 6. Compressive and flexural strength of TRM mortars at 7 and 28 days.

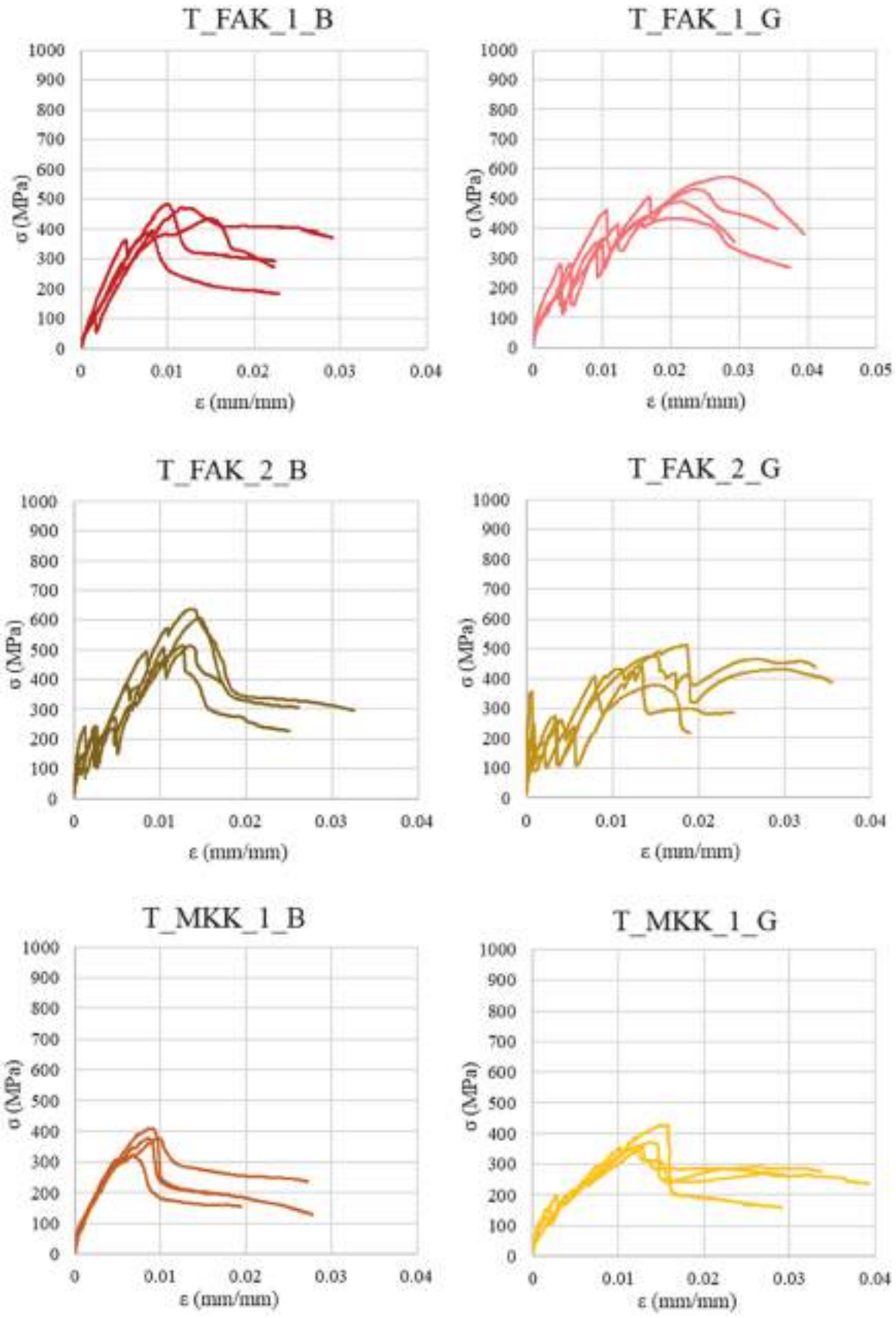

Fig. 7. Tensile tests: experimental stress-strain curves.

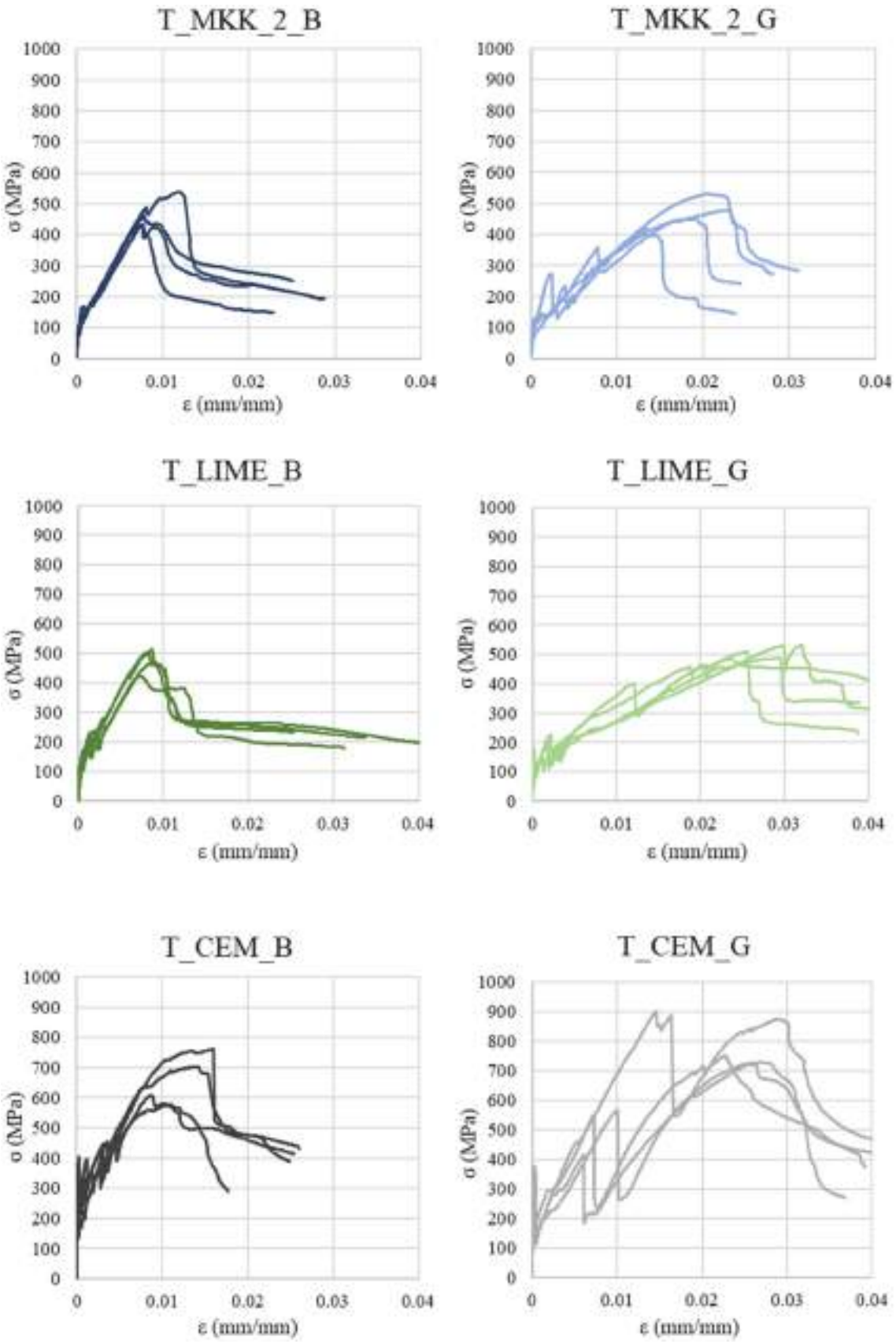

Fig. 7. (*continued*).

Table 6
Results of Tensile Tests.

Specimen		σ_1 (MPa)	$\sigma_{1,m}$ (MPa)	σ_{max} (MPa)	ε_{max}	Expl. ratio (%)	E_2 (GPa)	$\frac{\sigma_{f,m}}{\sigma_{1,m}}$	
T_FAK_1_B	Avg.	-	-	444	0.011	31.7	47.5	-	
	CoV	-	-	*9 %*	*24 %*				
T_FAK_1_G	Avg.	-	-	513	0.021	45.9	31.1	-	
	CoV	-	-	*9 %*	*27 %*				
T_FAK_2_B	Avg.	-	-	567	0.014	40.4	42.3	-	
	CoV	-	-	*11 %*	*7 %*				
T_FAK_2_G	Avg.	301	1.50	458	0.017	41.0	40.4	4.06	
	CoV	*46 %*	*46 %*	*10 %*	*22 %*				
T_MKK_1_B	Avg.	-	-	*370*	*0.009*	26.4	40.9	-	
	CoV	-	-	*10 %*	*15 %*				
T_MKK_1_G	Avg.	112	0.56	*376*	*0.014*	33.7	22.8	3.04	
	CoV	*35 %*	*35 %*	*9 %*	*12 %*				
T_MKK_2_B	Avg.	183	1.22	*465*	*0.009*	33.2	49.3	3.20	
	CoV	*33 %*	*33 %*	*10 %*	*24 %*				
T_MKK_2_G	Avg.	210	1.05	*466*	*0.019*	41.8	25.1	3.72	
	CoV	*39 %*	*39 %*	*11 %*	*20 %*				
T_Lime_B	Avg.	134	0.89	*476*	*0.008*	34.0	47.2	4.04	
	CoV	*17 %*	*17 %*	*8 %*	*8 %*				
T_Lime_G	Avg.	163	0.81	*503*	*0.028*	45.0	13.7	4.42	
	CoV	*19 %*	*19 %*	*5 %*	*13 %*				
T_Cem_B	Avg.	322	2.14	*661*	*0.012*	47.1	46.8	3.22	
	CoV	*23 %*	*23 %*	*13 %*	*25 %*				
T_Cem_G	Avg.	350	1.75	*776*	*0.022*	69.4	45.9	3.95	
	CoV	*20 %*	*20 %*	*11 %*	*24 %*				

reasonable to compare MKK with LIME and FAK with CEM mortars.

4.2. Tensile tests on TRM coupons

Tensile stresses are calculated by dividing the tensile load by the cross-sectional area of the reinforcing textile:

$$\sigma = \frac{F}{3A_Y}$$

where σ is the tensile stress in the textile, F is the applied tensile load and A_y is the cross-sectional area of a single yarn. σ_1 and $\sigma_{1,m}$ represent the tensile stress at first cracking in the textile or in the mortar, respectively. σ_{max} is the peak tensile stress while ε_{max} is the corresponding strain. σ_{max} was then compared to the tensile strength of the bare textile (from manufacturer) to obtain the exploitation ratio. The average modulus of elasticity in the post-cracking phase (E_2) was evaluated as the slope of the stress-strain curve between 0.6 and 0.9 of σ_{max}.

All the stress-strain curves are reported in Fig. 7. Each graph is named with the test type (T: tensile test) followed by the type of matrix and textile (G: glass, B: basalt). Stresses at first cracking (σ_1, $\sigma_{1,m}$), ultimate tensile strength (σ_{max}), ultimate tensile strain (ε_{max}), exploitation ratio and modulus of elasticity in the cracked phase (E_2) are reported in Table 6.

Stress-strain curves obtained from tensile tests on TRM coupons (Fig. 7) showed the typical behavior of these composites, that can be simplified in two or three quasi-linear phases [60–62]. However, for some specimens (T_FAK_1_B, T_FAK_1_G, T_MKK_1_B) it was not possible to identify the transition point (σ_1), which separates the pre- and post-cracking phases. This is probably due to some microcracks (not visible to the naked eye) already present in the specimens before testing, caused by the shrinkage of the geopolymer matrix during the curing phase. This phenomenon, also observed in other literature studies [19, 24,63], occurred especially in mortars with a high w/b ratio (FAK_1 and MKK_1), therefore more subjected to hygrometric shrinkage. These specimens showed a quasi-linear tensile behavior up to the maximum tensile stress (always greater than 350 MPa), with the opening of multiple cracks.

TRM with cement-based mortars (T_CEM_B and T_CEM_G) reached the highest tensile strength (661 and 776 MPa, respectively), corresponding to an average exploitation ratio of the bare textile equal to 47 % and 69 %, respectively. T_MKK_2 showed a tensile strength and modulus of elasticity comparable to those of lime-based systems. TRM based on fly ash mortars (FAK) showed a tensile strength comprised between those of MKK and CEM. Moreover, it is clear to observe that the modulus of elasticity in the cracked phase (E_2), being dependent on the modulus of elasticity of the reinforcing textile, it is always lower in the case of glass fiber mesh (G). The failure observed is always due to the slippage of the textile within the mortar, with the formation and opening of multiple cracks. Only in the case of cementitious matrices, for some specimens, the failure of internal yarns was observed. It is interesting to note that the stress at first cracking in the mortar ($\sigma_{m,1}$), when observable, can be correlated to the flexural strength of the mortars ($\sigma_{f,m}$). Their ratio ($\sigma_{f,m}/\sigma_{1,m}$) is always between 3.0 and 4.4.

DIC also allowed to monitor the evolution of the strain field and the formation of cracks over the free length of TRM coupons during tensile tests, as shown in Fig. 8. The maps show the vertical displacement and strain at various instants of time, until the maximum load is reached. It is interesting to observe that the number and average width of cracks vary for each specimen. In particular, FAK specimens showed the formation of 4 or 5 cracks before reaching the peak stress. The average cracks width was equal to 0.54, 0.95, 1.82 and 1.60 in the case of T_FAK_1_B, T_FAK_2_B, T_FAK_1_G and T_FAK_2_G, respectively. In the case of MKK specimens reinforced with basalt textile (T_MKK_1_B and T_MKK_2_B) a multi-cracking behavior is observed, with a greater number of smaller-amplitude cracks. This is probably due to the lower tensile strength of MKK matrices, which therefore crack more easily. For these specimens, generally only one crack propagates in the descending phase of the stress-strain curve. LIME specimens showed the formation of 4–6 cracks of greater amplitude in the case of glass textile reinforcement, while CEM specimens showed, on average, the formation of 2–4 cracks. The higher cracks opening of specimens reinforced with glass textiles is common for all matrix types. This is probably due to the lower modulus of elasticity of the fiberglass textile, compared to the basalt one. Furthermore, the different geometry of the cross-section of textile yarns, more flattened in the case of basalt yarns and more circular in the case of glass yarns (see Fig. 9), may have affected the stress transfer between matrices and yarn. Flattened yarns, having a greater surface/area ratio, allow a better stress transfer with the surrounding mortar.

Untested TRM coupons were cut to observe the cross-section with an optical microscope, at magnification of 6× (Fig. 9). It can be observed

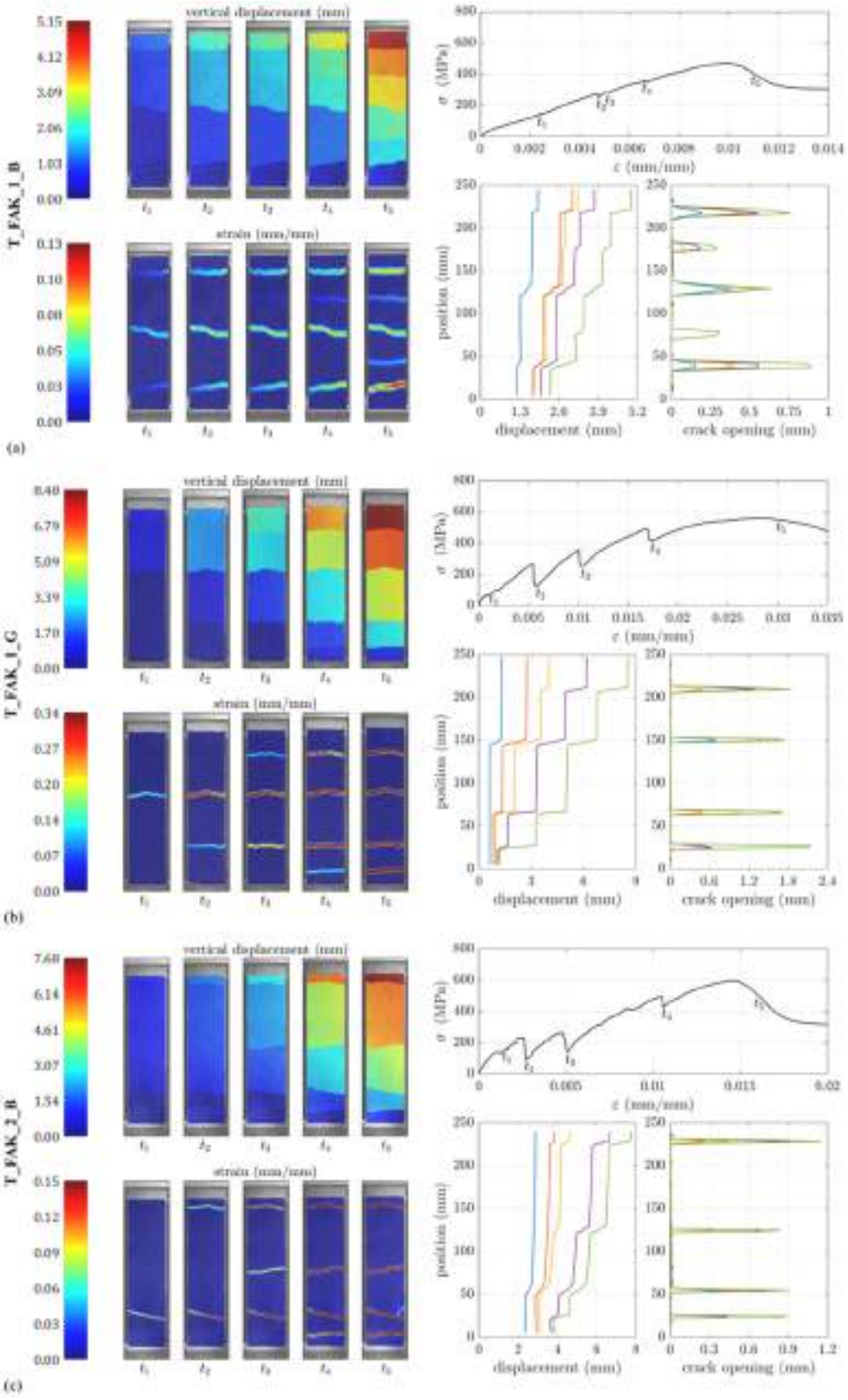

Fig. 8. TRM tensile tests: strain field evolution and cracks opening acquired through DIC.

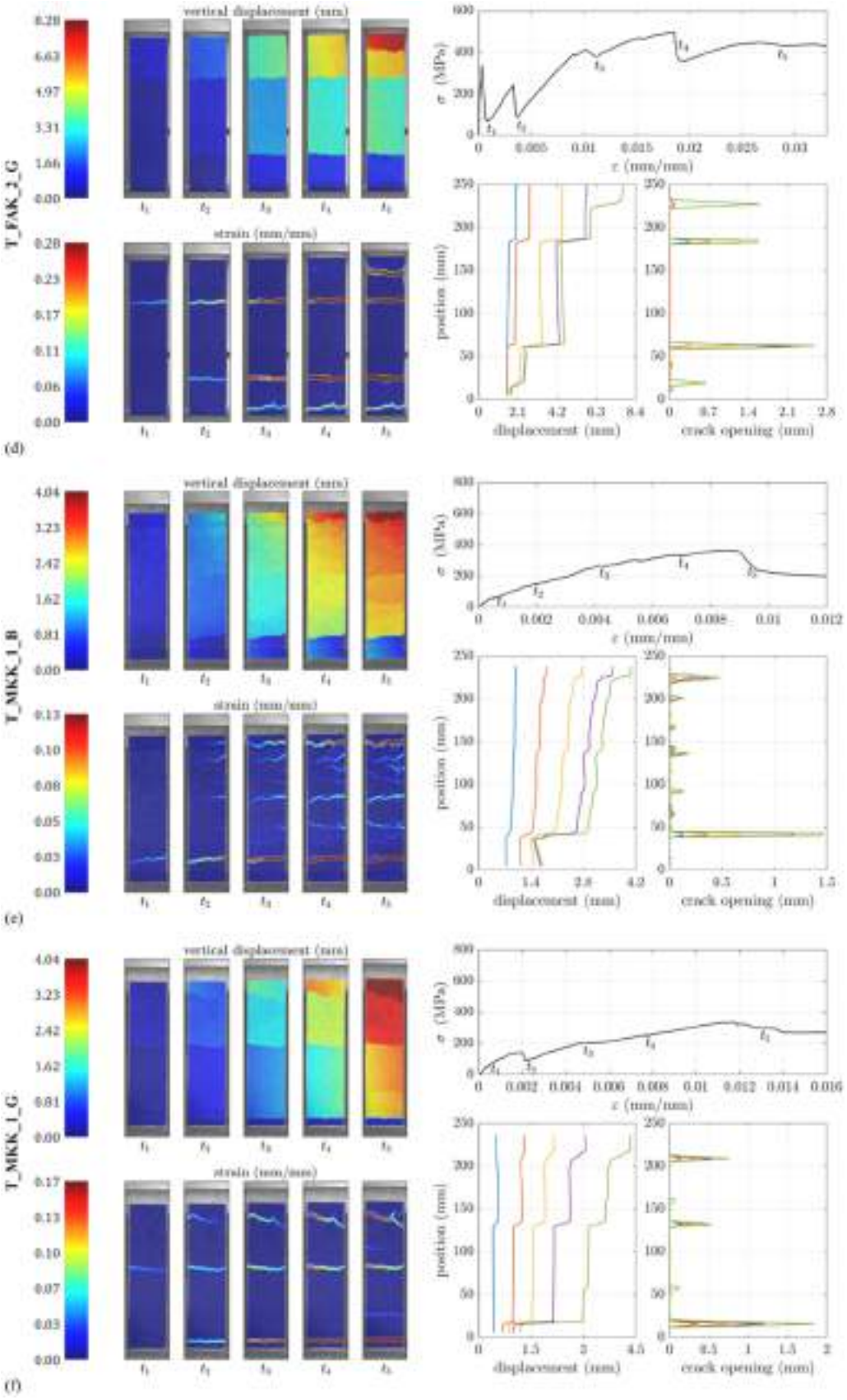

Fig. 8. (*continued*).

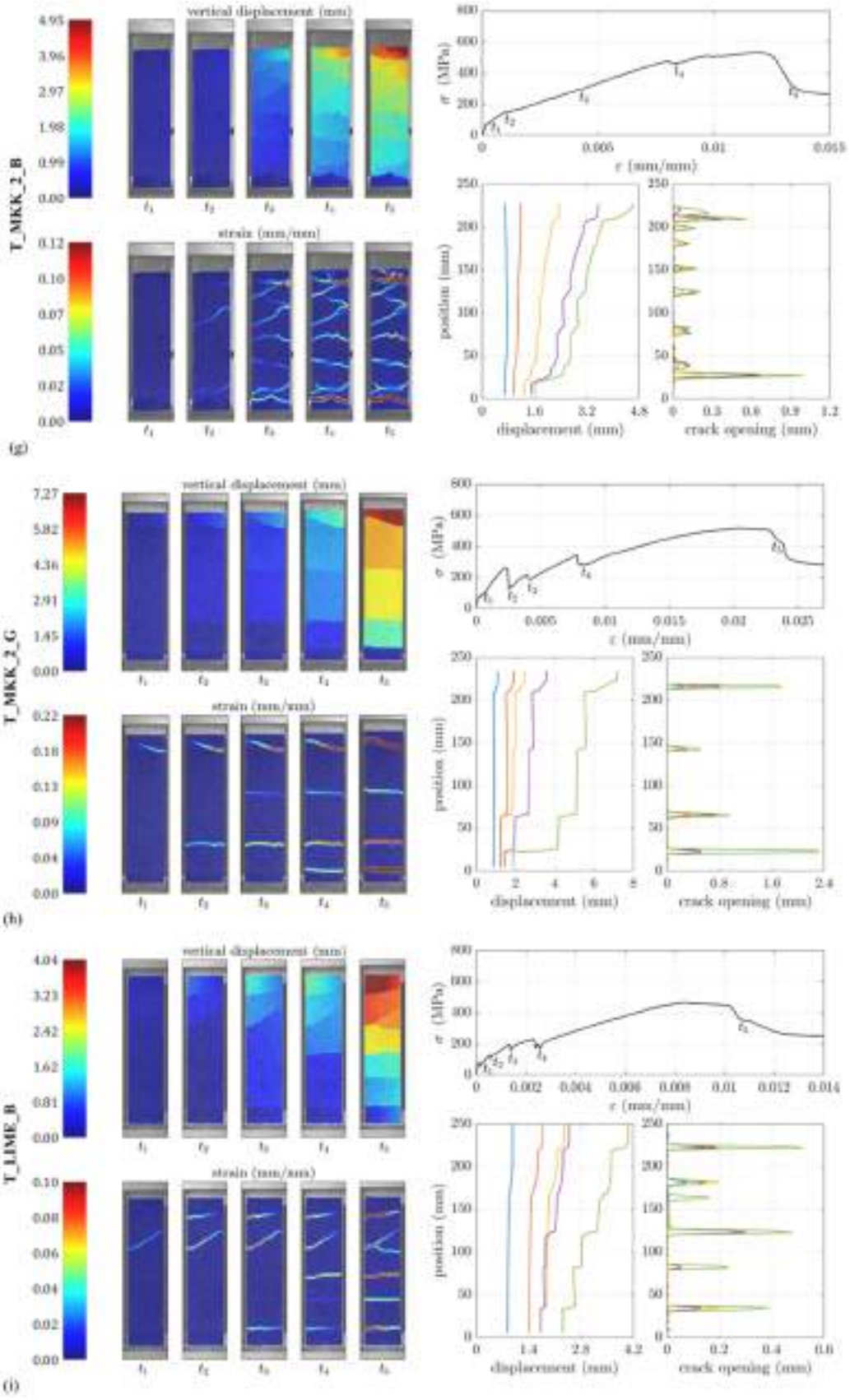

Fig. 8. (*continued*).

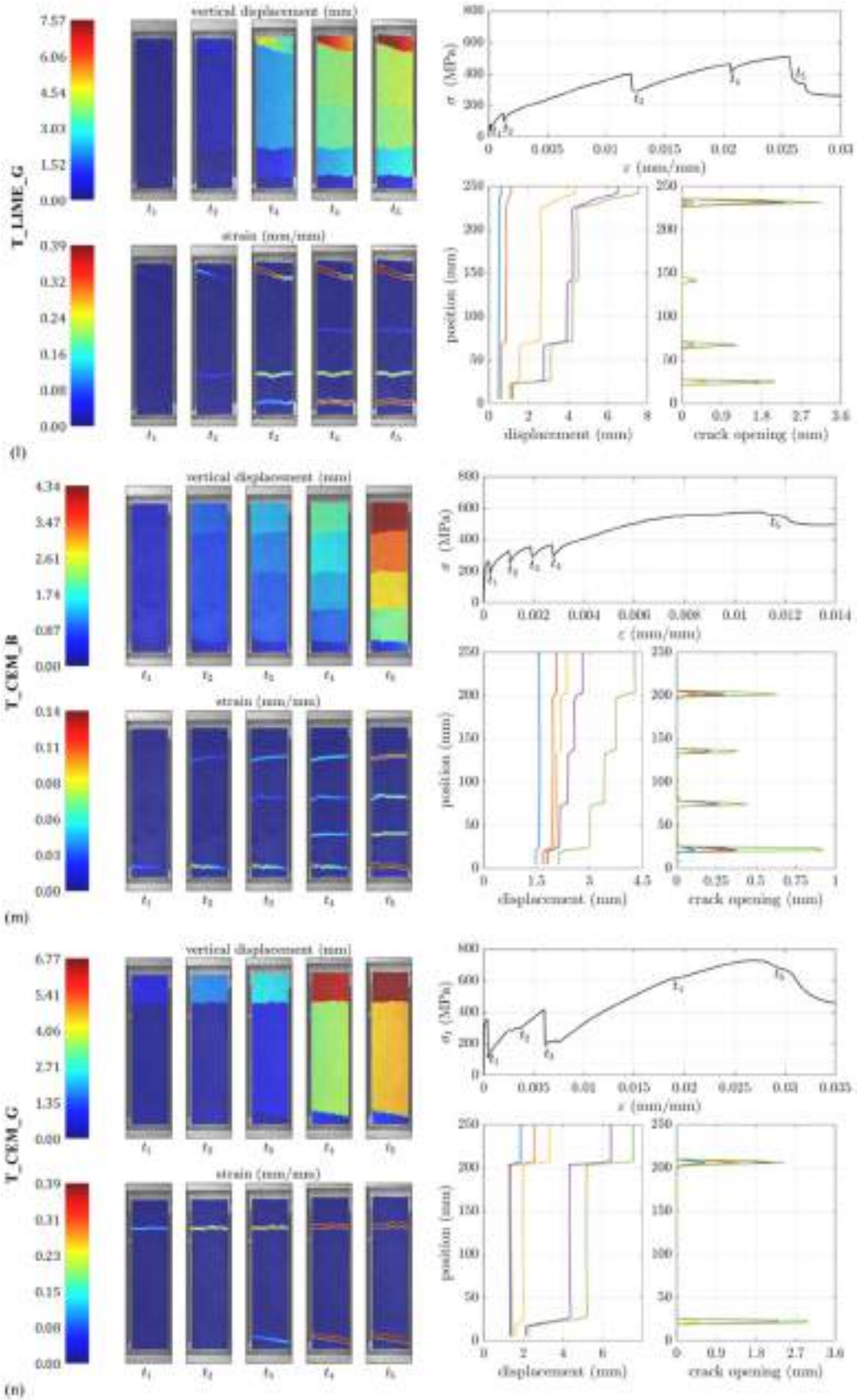

Fig. 8. (*continued*).

the different geometry of the yarns: basalt yarns (B) have an elongated and flat shape while glass yarns (G) have a more irregular geometry, and sometimes the presence of macro voids between filaments can be noted. This is probably due to the different pre-impregnation and production

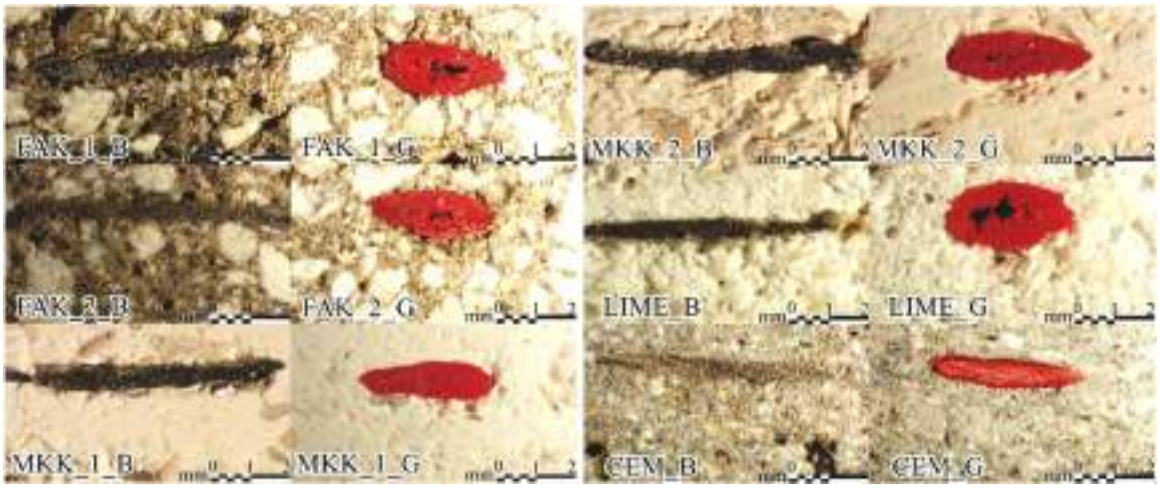

Fig. 9. Optical microscopy observations of the cross-section of TRM coupons.

method adopted by the manufacturer for the two types of textiles.

4.3. Single shear bond tests

The load-displacement curves of single shear bond tests are shown in Fig. 10 while a summary of key results is reported in Table 7. Each graph is named with the test type (SB: single-shear bond test) followed by the type of matrix and textile (B: basalt). The peak stress σ_u was calculated by dividing the peak load (F_{max}) by the nominal area of longitudinal yarns ($3A_y$). Relative displacement (δ) of the bare textile with respect to the clay brick substrate was evaluated through DIC. Failure modes observed for each type of specimens are reported in Fig. 11.

Alkali-activated matrices, both those based on fly ash (FAK) and metakaolin (MKK), showed excellent compatibility and a strong bond with the clay brick substrate, since the failure mode never involved the mortar-substrate interface. Failure occurred due to slippage of the textile within the mortar, and for some specimens (groups FAK_1_B and MKK_2_B) also involved the breakage of a single external yarn outside the bonded length, probably due to uneven stress distribution between yarns. In the case of lime-based mortar an interlaminar shear failure at the interface between mortar and fabric was observed.

The highest load values were achieved by specimens FAK_1_B, followed by FAK_2_B and MKK_2_B. All TRM systems based on alkali-activated matrices, except for the MKK_1_B, showed a peak stress in the textile (σ_u) higher than commercial systems. Cement-based TRM systems failed at low stress levels, due to premature detachment at the matrix-to-substrate interface (see Fig. 11). This is probably due to the high stiffness of the cementitious matrix, more suitable for reinforcing concrete elements rather than masonry. The exploitation ratio obtained in single shear tests was slightly higher for all specimens with respect to the corresponding one achieved during tensile tests (except for the cement matrix, due to premature detachment).

4.4. Energy and Environmental Indicators

In this section, the LCA results in terms of primary energy consumption and CO_2 emissions for the selected mixes and TRM systems are analyzed. Fig. 5 reported the required energy and GHG emission for each kg of adopted material. As expected, with the same mass, the glass and basalt textiles consume more energy and are liable for more emissions if compared with the other constituent materials. Considering just the constituent materials of the mortar, KOH is the most impactful and energy-intensive, followed by CAC.

In Fig. 12, a comparison of the different mortars is carried out in terms of EE and GWP indicators for cubic meter of mortar (Fig. 12a and b, respectively). The obtained values are in line with those obtained in other studies [41]. As expected, the CEM mortar has the highest impact and energy consumption, halving in some cases the performance of the other mortars.

It is well-known that lime is more sustainable than OPC [64], and this is also confirmed in the present study where the LIME mortar lowers both EE and GWP by more than 50 % compared to the CEM mortar. It is interesting that also AAMs have comparable EE and GWP values to those of the lime-based mortar, with FAK_1 having better environmental and energy performance than the others (even −50 % if compared with the LIME mortar in terms of EC). This is mainly due to the lower amount of KOH (if compared with FAK2 and MKK2) and the use of FA and CAC (instead of MKK if compared to MKK1 and MKK2), having an overall lower environmental impact and embodied energy than that of MKK.

In Fig. 13, the EE and GWP per square meters of the TRM system are reported. As can be seen, the glass and basalt fiber meshes are liable for the lower share of EE and GWP if compared with the share attributed to the mortars, except for the LIME_G and FAK_1_G cases, where the EE and GWP due to the fibers are equal to or higher than those due to the mortar, respectively. Again, among the TRM systems, those adopting the CEM mortar (CEM_B and CEM_G) have the highest impact. The FAK_1_B is the best performing in terms of both EE and GWP thanks to the highest energy and environmental performance of the mortar and fibers.

4.5. Efficiency analysis

To make a useful comparison between mortars and TRMs, it is important to consider the ratio obtained by the environmental/energy performance and the mechanical one (efficiency ratio, the lower the value, the better the mortar/TRM). In this way, the EE and GWP indicators are normalized, and the mortars can be compared in terms of functional unit, e.g. amount of material needed per unit of mechanical performance or the amount of EE/GWP needed to produce one unit of mechanical performance.

First, the mortars are compared by dividing the related EE and GWP indicators in Fig. 12 by compressive and flexural strength. The obtained values are shown in Figs. 14a and 14b, respectively. As can be seen, the most environmentally and energy-efficient mortar is still the FAK_1. This is thanks to the lowest value of EE and GWP (see Fig. 12) combined with the high compressive and flexural strength (see Fig. 6). Conversely, the less efficient one is the MKK_1. This is clearly due to the EE and GWP obtained for this mortar, higher than that of FAK_1, combined with the lowest compressive and flexural strength. Surprisingly, despite the highest value obtained in terms of EE and GWP, the CEM mortar has good efficiency ratios, still comparable with the value obtained for

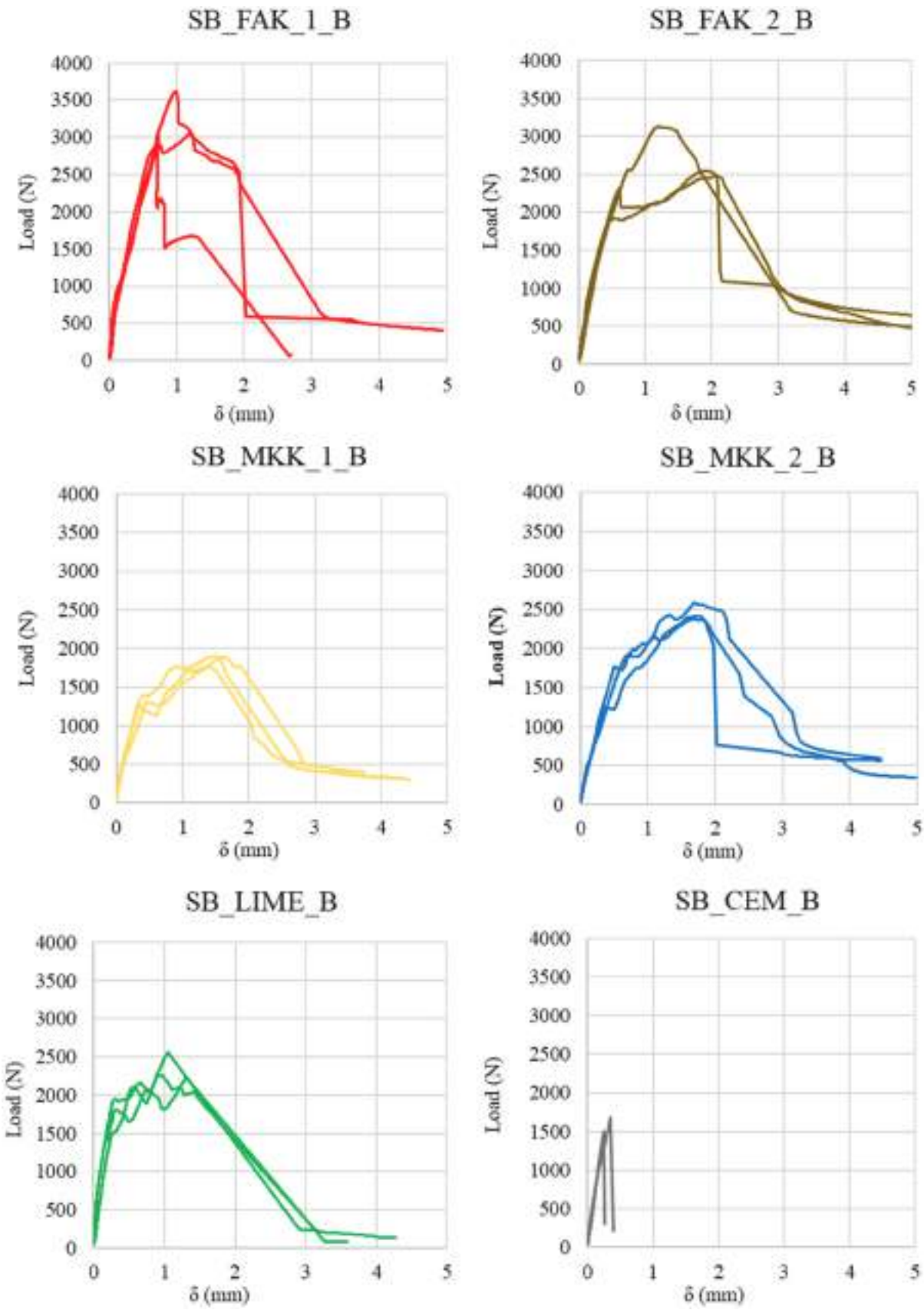

Fig. 10. Load-displacement curves of single-shear bond tests.

Table 7 –
Results of single-shear bond tests.

Specimen		Peak load F_{max} (N)	Peak stress σ_u (MPa)	Displacement at peak stress δ_{peak} (mm)	Expl. ratio (%)	Fail. mode
SB_FAK_1_B	Avg.	3243	813	0.98	58.0	D/E
	CoV	*10 %*	*10 %*	*24 %*		
SB_FAK_2_B	Avg.	2716	681	1.73	48.6	D
	CoV	*13 %*	*13 %*	*26 %*		
SB_MKK_1_B	Avg.	1851	464	1.49	33.1	D/E
	CoV	*4 %*	*4 %*	*8 %*		
SB_MKK_2_B	Avg.	2455	615	1.70	43.9	D/E
	CoV	*5 %*	*5 %*	*1 %*		
SB_LIME_B	Avg.	2348	589	1.10	42.0	C
	CoV	*8 %*	*8 %*	*17 %*		
SB_CEM_B	Avg.	1556	389	0.25	27.7	B
	CoV	*16 %*	*16 %*	*18 %*		

B: Detachment at the matrix-to-substrate interface
C: Debonding at the textile-to-matrix interface
D: Textile slippage within the matrix
E: Textile slippage within the matrix with cracking of the outer layer of mortar

FAK_2 and MKK_2, mainly thanks to its mechanical performance.

To compare the energy and environmental efficiency of the different TRM systems, the EE and GWP indicators plotted in Fig. 13 are divided by the related tensile and shear strengths. The obtained results are shown in Figs. 15a and 15b, respectively. Even in this case, the more efficient systems are those including the FAK_1 mortar, while the less efficient ones are those with MKK_1. Contrary to what observed in the mortar results (Fig. 14), this time the CEM-based TRM system shows a lower efficiency if compared with other TRMs. This is mainly due to the worst mechanical performance of the CEM when employed as TRM for masonry, especially considering the premature detachment of the mortar from the substrate and therefore the low shear bond strength.

5. Conclusions

This research aimed at evaluating the feasibility of employing alternative alkali-activated mortars (AAMs) in Textile Reinforced Mortar (TRM) systems. Four different AAMs, based on metakaolin (MKK) or fly ash (FAK), were developed as possible matrices for TRM systems, and their performances compared to those of lime- or cement-based commercial TRM systems. Comprehensive LCA and efficiency analysis were also performed on all matrices and TRM systems investigated.

The following key findings can be highlighted:

- Experimental results showed that AAMs, both FAK and MKK, could be a valid alternative to conventional lime- or cement-based mortars for TRM systems.
- Depending on the precursor used and the type and concentration of the alkaline activator, physical-mechanical properties of AAMs can be calibrated to reach similar performances of lime or cementitious mortars. Workability of AAMs was slightly higher than that of commercial matrices.
- The tensile behavior of TRAAM systems was similar to that of well-known commercial TRM based on lime or cementitious mortars. However, in some cases, especially for AAMs with higher w/b ratio (T_FAK_1 and T_MKK_1), the transition between the uncracked and cracked phase was not observed, probably due to the high

Fig. 11. Failure modes observed in shear bond tests.

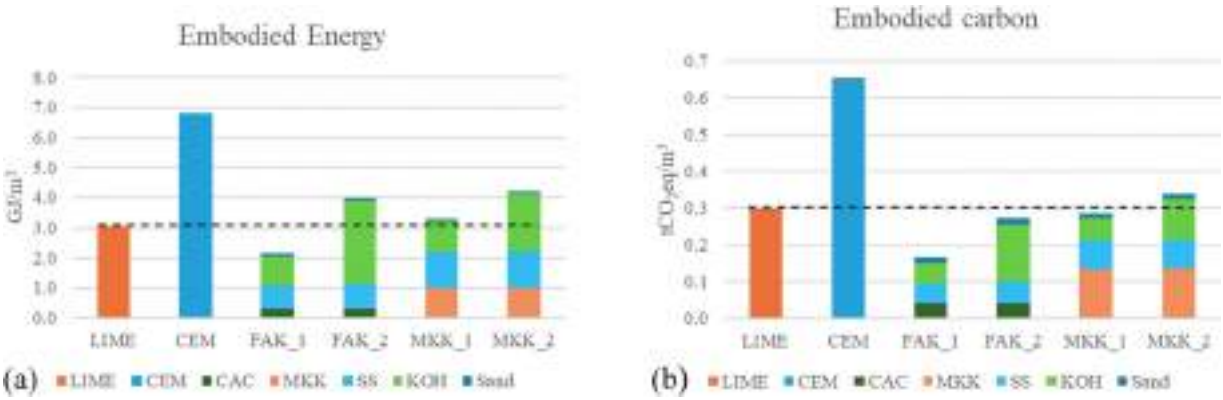

Fig. 12. a) EE and b) GWP per cubic meters of mortars. FA is not reported since having a negligible EE and GWP.

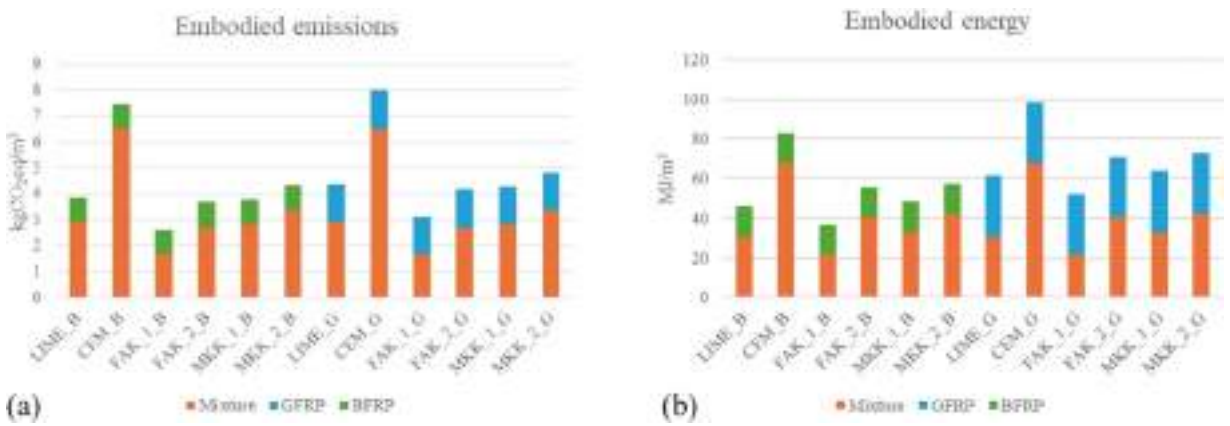

Fig. 13. a) EE and b) GWP per square meter of TRM systems.

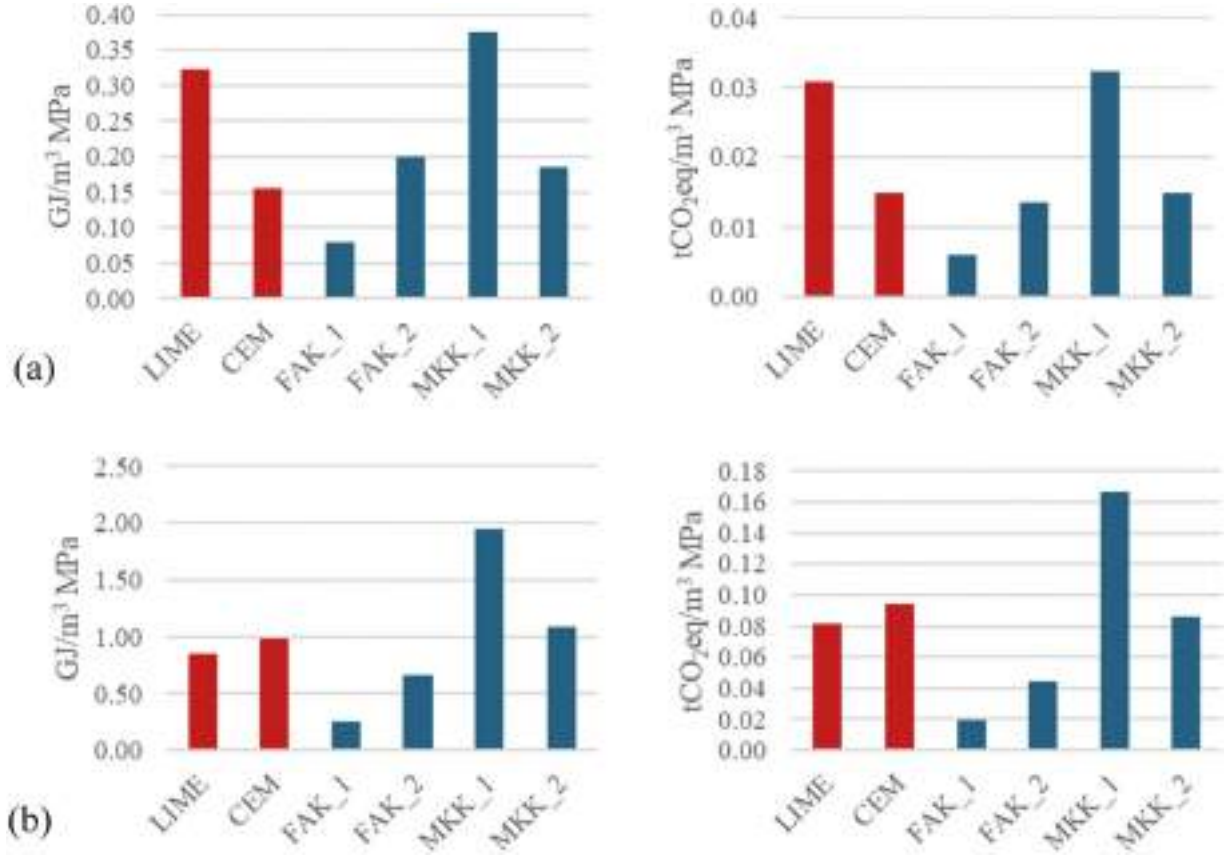

Fig. 14. Mortars energy and environmental efficiency ratios: EE and GWP per square meter normalized per unit of a) compressive strength and b) flexural strength.

hygrometric shrinkage of the matrices which could led to the formation of microcracks during the curing period.

- TRAAM coupons manufactured with FAK_1 and MKK_2 matrices showed tensile properties very similar to those obtained with commercial LIME mortar, while CEM specimens showed the highest tensile strength. However, the failure mode observed in tensile tests was always due to slippage of the textile within the matrix. Both polymeric coatings applied by the manufacturer on glass and basalt fibers (SBS and polyester-based, respectively), do not guarantee complete exploitation of the tensile properties of the reinforcements.
- AAMs demonstrated excellent adhesion to clay brick substrates. Failures observed in single-shear tests never occurred at the matrix-to-substrate interface. FAK_1 showed the best performances, with an exploitation ratio of 0.58, while CEM experienced premature failure, due to low bond between matrix and clay brick substrate.
- Regarding the environmental impact of newly developed AAMs and TRAAM systems, it is clear to observe that the choice of the precursor and the concentration of the alkaline activator play a fundamental role. The use of fly ash appears to be more interesting than metakaolin, both in terms of mechanical behavior as well as environmental/energy efficiency performances.

This research work has taken the first steps towards the use of AAMs for TRM strengthening systems. There is definitely still room for enhancing the performance of TRAAM systems, such as optimizing AAMs formulation to mitigate hygrometric shrinkage and developing

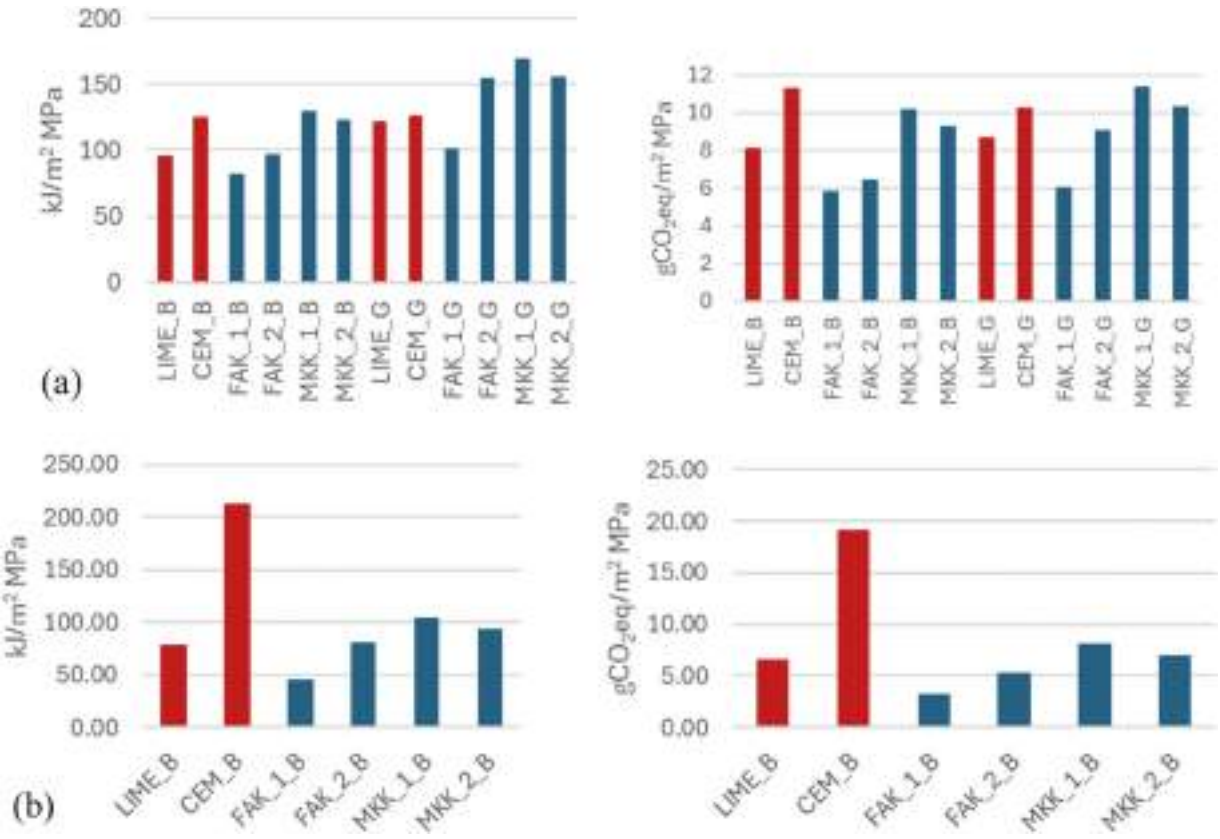

Fig. 15. TRM energy and environmental efficiency ratios: EE and GWP per square meter normalized per unit of a) tensile strength and b) shear strength.

new fiber coatings, more compatible with AAMs.

CRediT authorship contribution statement

Gianluca Chiappini: Writing – original draft, Investigation. **Francesca Tittarelli:** Supervision. **Alessandra Mobili:** Writing – original draft, Investigation. **Gianluca Maracchini:** Writing – review & editing, Writing – original draft, Methodology, Data curation. **Valeria Corinaldesi:** Supervision. **Jacopo Donnini:** Writing – review & editing, Writing – original draft, Resources, Methodology, Investigation, Data curation, Conceptualization.

Declaration of Competing Interest

The authors declare that they have no known competing financial interests or personal relationships that could have appeared to influence the work reported in this paper.

Data availability

Data will be made available on request.

Acknowledgements

Biemme Srl is gratefully acknowledged for providing the glass and basalt textiles.

References

[1] A. Nanni, A New Tool for Concrete and Masonry Repair, Concrete International, 2012.
[2] C. Papanicolaou, T. Triantafillou, K. Karlos, M. Papathanasiou, Textile-reinforced mortar (TRM) versus FRP as strengthening material of URM walls: in-plane cyclic loading, Mater. Struct. (2006).
[3] L.N. Koutas, Z. Tetta, D.A. Bournas, T.C. Triantafillou, Strengthening of concrete structures with textile reinforced mortars: state-of-the-art review, J. Compos. Constr. (2019), https://doi.org/10.1061/(ASCE)CC.1943-5614.0000882.
[4] J. Donnini, G. Maracchini, S. Lenci, V. Corinaldesi, E. Quagliarini, TRM reinforced tuff and fired clay brick masonry: experimental and analytical investigation on their in-plane and out-of-plane behavior, Constr. Build. Mater. 272 (2021), https://doi.org/10.1016/j.conbuildmat.2020.121643.
[5] J. Donnini, V. Corinaldesi, Mechanical characterization of different FRCM systems for structural reinforcement, Constr. Build. Mater. (2017), https://doi.org/10.1016/j.conbuildmat.2017.04.051.
[6] J. Donnini, V. Corinaldesi, A. Nanni, Mechanical properties of FRCM using carbon fabrics with different coating treatments, Compos B Eng. (2016), https://doi.org/10.1016/j.compositesb.2015.11.012.
[7] F. Bompadre, J. Donnini, Fabric-reinforced cementitious matrix (FRCM) carbon yarns with different surface treatments embedded in a cementitious mortar: mechanical and durability studies, Materials 15 (2022) 3927.
[8] P. Duxson, J.L. Provis, G.C. Lukey, J.S.J. van Deventer, The role of inorganic polymer technology in the development of "green concrete, Cem. Concr. Res 37 (2007), https://doi.org/10.1016/j.cemconres.2007.08.018.
[9] R. He, N. Dai, Z. Wang, Thermal and mechanical properties of geopolymers exposed to high temperature: a literature review, Adv. Civ. Eng. 2020 (2020), https://doi.org/10.1155/2020/7532703.
[10] P. Duxson, A. Fernández-Jiménez, J.L. Provis, G.C. Lukey, A. Palomo, J.S.J. Van Deventer, Geopolymer technology: the current state of the art, J. Mater. Sci. 42 (2007), https://doi.org/10.1007/s10853-006-0637-z.
[11] J.S.J. Van Deventer, J.L. Provis, P. Duxson, D.G. Brice, Chemical research and climate change as drivers in the commercial adoption of alkali activated materials, Waste Biomass Valoriz. 1 (2010), https://doi.org/10.1007/s12649-010-9015-9.
[12] B. Tempest, O. Sanusi, J. Gergely, V. Ogunro, D. Weggel, Compressive strength and embodied energy optimization of fly ash based geopolymer concrete. 3rd, World Coal Ash, WOCA Conf. - Proc. (2009).
[13] P. Zhang, Y. Zheng, K. Wang, J. Zhang, A review on properties of fresh and hardened geopolymer mortar, Compos B Eng. 152 (2018), https://doi.org/10.1016/j.compositesb.2018.06.031.
[14] G. Fahim Huseien, J. Mirza, M. Ismail, S.K. Ghoshal, A. Abdulameer Hussein, Geopolymer mortars as sustainable repair material: a comprehensive review, Renew. Sustain. Energy Rev. 80 (2017), https://doi.org/10.1016/j.rser.2017.05.076.
[15] Y.S. Wang, K.Di Peng, Y. Alrefaei, J.G. Dai, The bond between geopolymer repair mortars and OPC concrete substrate: strength and microscopic interactions, Cem. Concr. Compos 119 (2021), https://doi.org/10.1016/j.cemconcomp.2021.103991.
[16] S.K. John, Y. Nadir, K. Girija, Effect of source materials, additives on the mechanical properties and durability of fly ash and fly ash-slag geopolymer mortar:

a review, Constr. Build. Mater. 280 (2021), https://doi.org/10.1016/j.conbuildmat.2021.122443.
[17] J.N. Yankwa Djobo, A. Elimbi, H. Kouamo Tchakouté, S. Kumar, Mechanical properties and durability of volcanic ash based geopolymer mortars, Constr. Build. Mater. 124 (2016), https://doi.org/10.1016/j.conbuildmat.2016.07.141.
[18] J.L. Provis, Geopolymers and other alkali activated materials: why, how, and what? Mater. Struct. /Mater. Et. Constr. 47 (2014) https://doi.org/10.1617/s11527-013-0211-5.
[19] A. Arce, L. Azdejkovic, L. Miranda de Lima, C.G. Papanicolaou, T.C. Triantafillou, . Mechanical behavior of textile reinforced alkali-activated mortar based on fly ash, metakaolin and ladle furnace slag, Open Res. Eur. 2 (2022), https://doi.org/10.12688/openreseurope.14674.1.
[20] L. Carabba, M. Santandrea, C. Carloni, S. Manzi, M.C. Bignozzi, Steel fiber reinforced geopolymer matrix (S-FRGM) composites applied to reinforced concrete structures for strengthening applications: a preliminary study, Compos B Eng. 128 (2017), https://doi.org/10.1016/j.compositesb.2017.07.007.
[21] H.Y. Zhang, J. Yan, V. Kodur, L. Cao, Mechanical behavior of concrete beams shear strengthened with textile reinforced geopolymer mortar, Eng. Struct. 196 (2019), https://doi.org/10.1016/j.engstruct.2019.109348.
[22] S.K. John, Y. Nadir, N.K. Safwan, P.C. Swaliha, K. Sreelakshmi, V.A. Nambiar, Tensile and bond behaviour of basalt and glass textile reinforced geopolymer composites, J. Build. Eng. 72 (2023), https://doi.org/10.1016/j.jobe.2023.106540.
[23] S. Cholostiakow, L.N. Koutas, C.G. Papakonstantinou, Geopolymer versus cement-based textile-reinforced mortar: diagonal compression tests on masonry walls representative of infills in RC frames, Constr. Build. Mater. 373 (2023), https://doi.org/10.1016/j.conbuildmat.2023.130836.
[24] S. Candamano, F. Crea, A. Iorfida, Mechanical characterization of basalt fabric-reinforced alkali-activated matrix composite: a preliminary investigation, Appl. Sci. (Switz.) 10 (2020), https://doi.org/10.3390/APP10082865.
[25] S. Tamburini, M. Natali, E. Garbin, M. Panizza, M. Favaro, M.R. Valluzzi, Geopolymer matrix for fibre reinforced composites aimed at strengthening masonry structures, Constr. Build. Mater. 141 (2017), https://doi.org/10.1016/j.conbuildmat.2017.03.017.
[26] A. Mobili, C. Giosuè, M. Bitetti, F. Tittarelli, Cement mortars and geopolymers with the same strength class, Proc. Inst. Civ. Eng.: Constr. Mater. 169 (2016), https://doi.org/10.1680/coma.14.00063.
[27] A. Mobili, A. Belli, A. Telesca, M. Marroccoli, F. Tittarelli, Calcium sulfoaluminate and geopolymeric binders as alternatives to OPC, Am. Concr. Inst., Acids Spec. Publ. vol. 2018 (June, 2018).
[28] M.A. Sutton, J.H. Yan, V. Tiwari, H.W. Schreier, J.J. Orteu, The effect of out-of-plane motion on 2D and 3D digital image correlation measurements, Opt. Lasers Eng. (2008), https://doi.org/10.1016/j.optlaseng.2008.05.005.
[29] I. Jones, R. Bigger, B. Blaysat, C. Boo, M. Grewer, J. Hu, et al., A good practices guide for Digital Image Correlation, Int. Digit. Image Correl. Soc. (2018).
[30] M. Badaloni, M. Rossi, G. Chiappini, P. Lava, D. Debruyne, Impact of Experimental uncertainties on the identification of mechanical material properties using DIC, Exp. Mech. (2015), https://doi.org/10.1007/s11340-015-0039-8.
[31] D. Amodio, G.B. Broggiato, F. Campana, G.M. Newaz, Digital speckle correlation for strain measurement by image analysis, Exp. Mech. (2003), https://doi.org/10.1177/0014485103434004.
[32] F. Stazi, M. Serpilli, G. Chiappini, M. Pergolini, E. Fratalocchi, S. Lenci, Experimental study of the mechanical behaviour of a new extruded earth block masonry, Constr. Build. Mater. 244 (2020), https://doi.org/10.1016/j.conbuildmat.2020.118368.
[33] M. Simoncini, A. Forcellese, E. Mancini, G. Chiappini, M. Sasso, Experimental and numerical investigation on forming limit curves of AA6082 aluminum alloy at high strain rates, Int. J. Adv. Manuf. Technol. 112 (2021), https://doi.org/10.1007/s00170-020-06448-7.
[34] M. Sasso, E. Mancini, G. Chiappini, F. Sarasini, J. Tirillò, Application of DIC to static and dynamic testing of agglomerated cork material, Exp. Mech. 58 (2018), https://doi.org/10.1007/s11340-017-0369-9.
[35] G. Chiappini, M. Sasso, T. Bellezze, D. Amodio, Thermo-structural analysis of components in ceramic material, Procedia Struct. Integr. vol. 8 (2018), https://doi.org/10.1016/j.prostr.2017.12.061.
[36] G. Maracchini, G. Chiappini, J. Donnini, E. Quagliarini, V. Corinaldesi, S. Lenci, Application of digital image correlation to compression tests on tuff masonry panels strengthened by textile reinforced mortar, Int. J. Mason. Res. Innov. 1 (2022), https://doi.org/10.1504/ijmri.2022.10045349.
[37] M. Sasso, E. Mancini, G. Chiappini, M. Simoncini, A. Forcellese, Adapted Nakazima test to evaluate dynamic effect on strain distribution and dome height in balanced biaxial stretching condition, Int J. Mech. Sci. 148 (2018), https://doi.org/10.1016/j.ijmecsci.2018.08.024.
[38] F. Marchione, G. Chiappini, M. Rossi, C. Scoccia, P. Munafò, Experimental assessment of the static mechanical behaviour of the steel-glass adhesive joint on a 1:2 scale tensegrity floor prototype, J. Build. Eng. 53 (2022), https://doi.org/10.1016/j.jobe.2022.104572.
[39] A. Alsalman, L.N. Assi, R.S. Kareem, K. Carter, P. Ziehl, Energy and CO2 emission assessments of alkali-activated concrete and Ordinary Portland Cement concrete: a comparative analysis of different grades of concrete, Clean. Environ. Syst. 3 (2021) 100047, https://doi.org/10.1016/j.cesys.2021.100047.
[40] R. Frischknecht, N. Jungbluth, H.-J. Althaus, G. Doka, R. Dones, T. Heck, et al., The ecoinvent database: overview and methodological framework (7 pp), Int J. Life Cycle Assess. 10 (2005) 3–9, https://doi.org/10.1065/lca2004.10.181.1.
[41] A. Komkova, G. Habert, Environmental impact assessment of alkali-activated materials: examining impacts of variability in constituent production processes and transportation, Constr. Build. Mater. 363 (2023) 129032, https://doi.org/10.1016/j.conbuildmat.2022.129032.
[42] S. Oyebisi, T. Alomayri, Cement-based concrete modified with Vitellaria paradoxa ash: a lifecycle assessment, Constr. Build. Mater. 342 (2022) 127906, https://doi.org/10.1016/j.conbuildmat.2022.127906.
[43] L. Assi, K. Carter, E. (Eddie Deaver, R. Anay, P. Ziehl, Sustainable concrete: building a greener future, J. Clean. Prod. 198 (2018) 1641–1651, https://doi.org/10.1016/j.jclepro.2018.07.123.
[44] T. Stengel, J. Reger, D. Heinz, Life cycle assessment of geopolymer concrete – what is the environmental benefit, Concr. Solut. 09 (2009) 1–10.
[45] R. Jones, M. Mccarthy, M. Newlands, Fly ash route to low embodied CO 2 and implications for concrete construction, WOCA Proc. Pap. (2011) 1–14.
[46] The Concrete Centre. The concrete industry sustainability performance 1st report. Camberley, Surrey GU17 9AB: 2009.
[47] A. Heath, K. Paine, M. McManus, Minimising the global warming potential of clay based geopolymers, J. Clean. Prod. 78 (2014) 75–83, https://doi.org/10.1016/j.jclepro.2014.04.046.
[48] Mehta P.K., Monteiro P.J.M. Concrete: Microstructure, Properties, and Materials. third ed. New York: McGraw-Hill; 2006.
[49] B. Tempest, O. Sanusi, J. Gergely, V. Ogunro, D. Weggel, Compressive strength and embodied energy optimization of fly ash based geopolymer concrete. 3rd World of Coal Ash, WOCA Conf. - Proc. (2009) 1–17.
[50] G. Hammond, Jones C., Lowrie F., Tse P. Building Services Research and Information Association. 2011.
[51] L.K. Turner, F.G. Collins, Carbon dioxide equivalent (CO2-e) emissions: a comparison between geopolymer and OPC cement concrete, Constr. Build. Mater. 43 (2013) 125–130, https://doi.org/10.1016/j.conbuildmat.2013.01.023.
[52] M. Fawer, M. Concannon, W. Rieber, Life cycle inventories for the production of sodium silicates, Int. J. Life Cycle Assess. 4 (1999) 207–212, https://doi.org/10.1007/BF02979498.
[53] G.P. Hammond, C.I. Jones, Embodied energy and carbon in construction materials, Proc. Inst. Civ. Eng.: Energy 161 (2008) 87–98, https://doi.org/10.1680/ener.2008.161.2.87.
[54] B.C. McLellan, R.P. Williams, J. Lay, A. Van Riessen, G.D. Corder, Costs and carbon emissions for geopolymer pastes in comparison to ordinary portland cement, J. Clean. Prod. 19 (2011) 1080–1090, https://doi.org/10.1016/j.jclepro.2011.02.010.
[55] L.N. Assi, K. Carter, E. Deaver, P. Ziehl, Review of availability of source materials for geopolymer/sustainable concrete, J. Clean. Prod. 263 (2020), https://doi.org/10.1016/j.jclepro.2020.121477.
[56] Davidovits J. False Values on CO2 Emission for Geopolymer Cement/concrete Published in Scientific Papers. n.d.
[57] A. Akbar, K.M. Liew, Multicriteria performance evaluation of fiber-reinforced cement composites: an environmental perspective, Compos B Eng. 218 (2021) 108937, https://doi.org/10.1016/j.compositesb.2021.108937.
[58] A. Borri, M. Corradi, R. Sisti, C. Buratti, E. Belloni, E. Moretti, Masonry wall panels retrofitted with thermal-insulating GFRP-reinforced jacketing, Mater. Struct. /Mater. Et. Constr. 49 (2016), https://doi.org/10.1617/s11527-015-0766-4.
[59] F. Longo, P. Lassandro, A. Moshiri, T. Phatak, M.A. Aiello, K.J. Krakowiak, Lightweight geopolymer-based mortars for the structural and energy retrofit of buildings, Energy Build. 225 (2020), https://doi.org/10.1016/j.enbuild.2020.110352.
[60] D. Arboleda, F.G. Carozzi, A. Nanni, C. Poggi, Testing procedures for the uniaxial tensile characterization of fabric-reinforced cementitious matrix composites, J. Compos. Constr. (2016), https://doi.org/10.1061/(ASCE)CC.1943-5614.0000626.
[61] J. Donnini, F. Bompadre, V. Corinaldesi, Tensile behavior of a glass FRCM system after different environmental exposures, Processes 8 (2020), https://doi.org/10.3390/pr8091074.
[62] J. Donnini, G. Chiappini, G. Lancioni, V. Corinaldesi, Tensile behaviour of glass FRCM systems with fabrics' overlap: experimental results and numerical modeling, Compos Struct. (2019), https://doi.org/10.1016/j.compstruct.2019.01.053.
[63] A. Mobili, C. Giosuè, A. Belli, T. Bellezze, F. Tittarelli, Geopolymeric and cementitious mortars with the same mechanical strength class: performances and corrosion behaviour of black and galvanized steel bars, Am. Concr. Inst., Acids Spec. Publ. vol. 2015 (January, 2015).
[64] J. Válek, E. Van Halem, A. Viani, M. Pérez-Estébanez, R. Ševčík, P. Šašek, Determination of optimal burning temperature ranges for production of natural hydraulic limes, Constr. Build. Mater. 66 (2014), https://doi.org/10.1016/j.conbuildmat.2014.06.015.